NAVAL POSTGRADUATE SCHOOL
Monterey, California

AD-A284 636

THESIS

FIRST PRINCIPLES USED IN ORBITAL PREDICTION

AND AN ATMOSPHERIC MODEL COMPARISON

By

Brian E. Bowden

June 1994

Thesis Advisor: R. C. Olsen

Approved for public release; distribution is unlimited

DTIC QUALITY INSPECTED 3

94-29313

REPORT DOCUMENT PAGE

Public reporting burden for this collection of information is estimated to average 1 hour per response, including the time for reviewing instructions, searching existing data sources, gathering and maintaining the data needed, and completing and reviewing the collection of information. Send comments regarding this burden estimate or any other aspect of this collection of information, including suggestions for reducing this burden, to Washington Headquarters Services, Directorate for Information Operations and Reports, 1215 Jefferson Davis Highway, suite 1204, Arlington, VA 22202 - 4302, and to the Office of Management and Budget, Paperwork Reduction Project (0704-0188) Washington, DC 20503

1. AGENCY USE ONLY (Leave Blank)	2. REPORT DATE	3. REPORT TYPE AND DATES COVERED
	16 JUNE 1994	Master's Thesis

4. TITLE AND SUBTITLE

FIRST PRINCIPLES USED IN ORBITAL PREDICTION AND AN ATMOSPHERIC MODEL COMPARISON

5. FUNDING NUMBERS

6. AUTHORS

Bowden, Brian E.

7. PERFORMING ORGANIZATION NAME(S) AND ADDRESS(ES)

Naval Postgraduate School

Monterey, CA 93943-5000

8. PERFORMING ORGANIZATION REPORT NUMBER

9. SPONSORING / MONITORING AGENCY NAME(S) AND ADDRESS(ES)

10. SPONSORING / MONITORING AGENCY REPORT NUMBER

11. SUPPLEMENTARY NOTES

The views expressed in this thesis are those of the author and do not reflect the official policy or position of the Department of Defense or the U. S. Government.

12a. DISTRIBUTION / AVAILABILITY STATEMENT

Approved for public release, distribution is unlimited.

12b. DISTRIBUTION CODE

13. ABSTRACT (MAXIMUM 200 WORDS)

This thesis develops an orbital prediction model based on fundamental principles of orbital dynamics and drag. A FORTRAN based orbital prediction scheme was designed to provide accurate ephemerides for a particular DoD satellite program. The satellite program under study has satellites at 650 and 800 kilometers with high inclinations. In order to obtain the highest accuracy possible, a comparison of atmospheric models had to be conducted in order to determine which model was more accurate. Mathematical formulation for three widely used earth atmospheric models are presented; the JACCHIA 60, JACCHIA 71, and MSIS 86 atmospheric models. The MSIS 86 atmospheric model was not evaluated due to computer problems. Comparison of the two JACCHIA models proved that the JACCHIA 71 model provided much more accurate ephemerides. It is believed that this is due not only to the incorporation of variations in density caused by solar flux, but also geomagnetic activity and a better modeling of the polar regions. Further work on this project would include incorporation of the MSIS 86 model for evaluation, incorporation of the full WGS-84 geopotential model, and using more accurate observed vectors in order to obtain a better comparison. Incorporating a subroutine which will vary the B-factor as a function of latitude will greatly increase accuracy. This is a major deviation from current operational practice, in that the B-factor is often used as an error catch-all and does not truly represent its dynamical purpose.

14. SUBJECT TERMS

Atmospheric Models, Orbital Prediction, atmosphere, thermospheric processes, B-factor, solar flux, geomagnetic activity, density

15. NUMBER OF PAGES

83

16. PRICE CODE

17. SECURITY CLASSIFICATION OF REPORT	18. SECURITY CLASSIFICATION OF THIS PAGE	19. SECURITY CLASSIFICATION OF ABSTRACT	20. LIMITATION OF ABSTRACT
UNCLASSIFIED	UNCLASSIFIED	UNCLASSIFIED	UL

NSN 7540-0 1-280-5500

Standard Form 298 (Rev. 2-89)
Prescribed by ANSI Std. Z39-18
298-102

DTIC QUALITY INSPECTED 3

First Principles Used in Orbital Prediction

and an Atmospheric Model Comparison

by

Brian E. Bowden
Lieutenant , United States Navy
B.S., The Military College of South Carolina, 1986

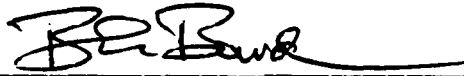Submitted in partial fulfillment

of the requirements for the degree of

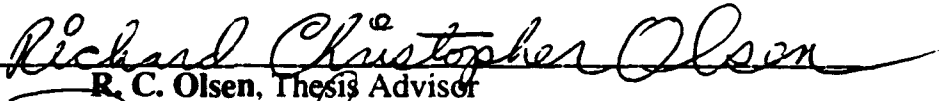**MASTER OF SCIENCE IN ASTRONAUTICAL ENGINEERING**

from the

NAVAL POSTGRADUATE SCHOOL
June 16, 1994

Author: _____

Brian E. Bowden

Approved by: _____

R. C. Olsen, Thesis Advisor

_____

R. L. Wight, Second Reader.

_____

Daniel J. Collins, Chairman, Department of
Aeronautics and Astronautics

ii

ABSTRACT

This thesis dev   an orbital prediction model based on fundamental principles of orbital dynamics and drag. A FORTRAN based orbital prediction scheme was designed to provide accurate ephemerides for a particular DoD satellite program. The satellite program under study has satellites at 650 and 800 kilometers with high inclinations. In order to obtain the highest accuracy possible, a comparison of atmospheric models had to be conducted in order to determine which model was more accurate. Mathematical formulation for three widely used earth atmospheric models are presented; the JACCHIA 60, JACCHIA 71, and MSIS 86 atmosphe   s. The MSIS 86 atmospheric model was not evaluated due to computer problems. Comparison of the two JACCHIA models proved that the JACCHIA 71 model provided much more accurate ephemerides. It is believed that this is due not only to the incorporation of variations in densi.y caused by solar flux, but also geomagnetic activity and a better modeling of the polar regions. Further work on this project would include incorporation of the MSIS 86 model for evaluation, incorporation of the full WGS-84 geopotential model, and using more accurate observed vectors in order to obtain a better comparison. Incorporating a subroutine which will vary the B-factor as a function of latitude will greatly increase accuracy. This is a major deviation from current operational practice, in that the B-factor is often used as an error catch-all and does not truly represent its dynamical purpose.

iii

TABLE OF CONTENTS

ACKNOWLEDGMENT

I. INTRODUCTION

Orbital prediction has become an essential science needed for several of the DoD satellite programs. Exact satellite ephemerides provide for a more accurate means of mission analysis. Put more directly, the more accurate the satellite ephemerides can be calculated or predicted, the more accurate the mission analysis becomes. The main objective being to pinpoint the satellites current or future position. Since the launch of Sputnik in the late fifties, a great deal of effort has been placed in trying to model the space environment. In particular, the upper atmosphere, or neutral atmosphere, has been of great interest in the study of artificial satellite orbit theory. Since 1957, several attempts have been made in modeling the thermosphere in order to aid in satellite mission analysis. Several atmospheric models, or satellite drag models, are currently used for practical applications such as lifetime estimates, reentry prediction, orbit determination and tracking, attitude dynamics, and most recently, mass analysis of a particular satellite. Atmospheric drag affects all satellites, in all altitude regimes, from low earth orbits to well beyond geosynchronous altitudes. For many satellites, the modeling of atmospheric drag is the largest error source in describing the forces acting on the satellite.

Satellite drag models can be divided into two categories, the empirical models and the general circulation models. This thesis will compare three of the more widely used empirical models. The models used for the comparison are the Jacchia 60, the Jacchia 71, and the MSIS 86 earth atmospheric models. Each of these models is formulated in a different manner and are unique for the altitude bands that were tested. The ultimate goal being to find out which model is more accurate in terms of orbit prediction for a particular satellite program. Since the modeling of atmospheric drag is the largest error in orbital

1

prediction, finding the more accurate model for the satellite program in question will greatly improve the predicted satellite ephemirides and hence mission analysis.

The atmospheric models being used in this comparison all differ with respect to the input that each model requires. Currently the Air Force Satellite Tracking Center (STC) uses the Jacchia 60 atmospheric model which uses not only date and time as inputs but also the measurement of the solar flux, $F10.7$. The J71 model, considered to be an improvement of the Jacchia 60 model, adds the measurement of geomagnetic activity, or Ap, to its inputs. The MSIS 86 atmospheric model is formulated in a different manner than the Jacchia atmospheric models, and uses both $F10.7$, and Ap as its inputs.

The atmospheric models calculate the density and constituency of the atmosphere based on the current and predicted or average environmental conditions. The accuracy of these models has been calculated to be 80 to 85 percent accurate. This percentage drops off substantially as the altitude increases. Accuracy also seems to decrease during periods of high solar and geomagnetic activity. At the moment, the sun is on the downside of the 11 year solar cycle. This is an advantage for the comparison of the atmospheric models, because there were fewer and weaker solar flares and geomagnetic storms to perturb the upper atmosphere.

II. BACKGROUND

A. ATMOSPHERE

The earth's atmosphere is classically divided into four different regions based on temperature and pressure gradients. These four regions are the troposphere, stratosphere, mesosphere and the thermosphere. The corresponding boundary layers, or upper limits of each of the regions are the tropopause, stratopause, mesopause, and thermopause respectively. Figure 1 (Akasofu, 1972, p.109), illustrates the breakdown of the earth's atmospheric regions. Beyond the thermopause is the region delineated as the exosphere. The exosphere is a region of extremely low density and temperature, and is the transition region into space.

Another way in which the earth's atmosphere is divided, is by the classification of two regions known as the homosphere and the heterosphere. The transition boundary between the regions is labeled the turbopause. Once again the region outside the heterosphere is labeled the exosphere. Figure 2 (Akasofu, 1972, p.111) illustrates the various atmospheric regions as derived by the two defining systems. This figure provides a breakdown of altitude versus temperature for the various altitude regimes. It should be noted at this time, that the atmospheric region of interest during this study was an altitude band between 600 to 800 km. This altitude band is encompassed within either the thermosphere or exosphere, depending on which classification scheme is being used. For the sake of continuity, the altitude band of interest will be considered to be within the thermosphere.

1. Troposphere

The troposphere is that portion of the atmosphere that extends from the surface to roughly 10 to 15 km above the surface. It is in equilibrium with the sun-warmed surface and is characterized by intense convection and cloud formations. In this region, both temperature and density decrease with increasing altitude, with an occasional inversion layer. (U.S. Air Force, 1960, p.1-3)

2. Stratosphere

The stratosphere is located above the tropopause and extends up to 50 km. This region of the atmosphere is extremely important in that it contains the ozone that is responsible for the absorption of the extreme ultraviolet (EUV) radiation produced by the sun. Due to the absorption of this EUV radiation, the stratosphere has a positive temperature gradient. The density, however, still decreases with altitude. One other consequence of the absorption of the EUV radiation by the ozone layer is that the EUV radiation cannot be measured from the earth's surface. This presents a problem which will be addressed later in this paper.

3. Mesosphere

The Mesosphere is that region of the atmosphere located above the stratopause and extends up to 80km. Once again, both the temperature and density are decreasing with altitude. The mesosphere is in radiative equilibrium between the ultraviolet ozone heating by the upper fringe of the stratosphere, and the infrared ozone and carbon dioxide cooling by radiation to space. (U.S. Air Force, 1960, p.1-3)

4. Thermosphere

The thermosphere extends from the mesopause to higher altitudes with no altitude limit. The thermosphere is characterized by a very rapid increase in temperature

4. Thermosphere

The thermosphere extends from the mesopause to higher altitudes with no altitude limit. The thermosphere is characterized by a very rapid increase in temperature with altitude due to the absorption of the sun's EUV radiation. The temperature increase reaches a limiting value known as the exospheric temperature, the average values being between ~600 to 1200 K over a solar cycle. (Larson, 1992, p.208) The thermosphere may also be heated by geomagnetic activity, which transfers energy from the magnetosphere and ionosphere to the thermosphere. The heating of the thermosphere causes an increase in the atmospheric density due to the expansion of the atmosphere. Figure 3 (Hess, 1965, p. 679), illustrates the variation of temperature versus altitude for the various atmospheric regimes.

5. Homosphere

The homosphere extends from the surface to approximately 100km. It is characterized by its uniform composition and relatively constant molecular weight. The composition of this region can be broken down into the following: 78% N, 21% O_2, 1% Ar and trace amounts of other gases. The uniformity of the region is created due to the turbulent mixing of the gas constituents. (Adler, 1993, p.10) The composition, hence the uniformity, of the homosphere changes at ~100km altitude due mainly to the dissociation of the oxygen molecules. Because the density at this altitude is low, recombination of the monatomic oxygen is very infrequent; even more so as altitude increases. The dissociation of oxygen causes the molecular weight to decrease substantially.

6. Heterosphere

The heterosphere exists from ~ 100km outward, with no altitude limit. The region is characterized by diffusive equilibrium and significantly varying composition. The

molecular weight of the atmosphere decreases rapidly, from ~ 29 at 90km to ~ 16 at 500km. Above the region of oxygen dissociation, nitrogen begins to dissociate. Diffusive equilibrium begins to take place, and the lighter molecules and atoms rise to the top of the atmosphere. The distribution functions, or scale heights. of each of the constituents of the heterosphere are found b) equating the pressure gradient of the atmosphere with the gravitational force, as described by the ideal gas law,

$$p = \left(\frac{\rho}{m}\right)kT \qquad (1)$$

where p = gas pressure, k = Boltzman constant, m = molecular mass, T = temperature, and ρ = density. For a small cross sectional area of thickness dh

$$dP = -\rho g dh \qquad (2)$$

therefore

$$\frac{dP}{P} = \frac{d\rho}{\rho} + \frac{dT}{T} \qquad (3)$$

$$-dh = \frac{kT}{mg}\left(\frac{d\rho}{\rho} + \frac{dT}{T}\right) \qquad (4)$$

By assuming isothermal variation and defining the scale height to be $H = \dfrac{kT}{mg}$, a simple differential equation is obtained described by the following;

$$\frac{d\rho}{\rho} = -\frac{1}{H}dh \qquad (5)$$

with the solution being;

$$\rho = \rho_o e^{-\frac{1}{H}h} \qquad (6)$$

Each molecule will have a different scale height depending upon its mass. This gives rise to diffusive equilibrium, in that the density of the varying constituents will decrease at

certain levels. The diffusion process takes place amongst Ar, O_2, N_2, O, He, and H respectively as altitude increases. (Adler, 1992, p.11) Figure 4 (Akasofu, 1972, p. 110) illustrates the densities of the various atmospheric constituents versus altitude.

7. Time Dependent Variations

Several time dependent density variations are present in the earth's atmosphere. The density of the earth's atmosphere varies according to the time of day, day of the year, and which year it happens to be in the 11 year solar cycle.

a. Diurnal Variation

The atmospheric density variation which is dependent upon the time of day is called the diurnal variation. The maximum density of the upper atmosphere can be found at approximately 1400 local time, with the minimum around 0200 local time. The density variation becomes more pronounced with an increase in altitude as can be seen in Figure 5. (Hess, 1968, p. 99) The diurnal variation is caused by the alternate heating during the day and cooling during the night of the upper atmosphere. Often called the diurnal bulge, the density variation occurs mainly over the equator, with an elongation in the north-south direction due to the tilt of the ecliptic. The peak of the phenomena occurs at the latitude of the sub-solar point. (Jacchia, 1963, p. 983) The temperature change in the upper atmosphere during this diurnal correction parallels that of the density, except that the temperature change lags behind the density change by approximately two hours. This lag seems opposite of what would be expected, and is not completely understood.

b. 27-day Variations

It has been established that there is a density variation that is caused by the 27-day solar cycle. This was shown by Jacchia, who determined the correlation between actual satellite drag measurements and the solar decimetric flux, or 10.7 cm flux. It was

found that the density of the atmosphere not only had a daily variation, but also a monthly, or 27 day cycle, that corresponded to the 27 day rotation cycle of the sun. (Hess, 1968, p.101)

c. Semi-Annual Variations

One of the least understood upper atmosphere density variations is the semi-annual variation. This density variation is characterized by a pronounced minimum during the June-July time frame, with a secondary minimum occurring in January. The maximums occur during the September-October time frame, with a lesser secondary maximum occurring during March-April. Several theories exist as to what causes the semi-annual variation. The most controversial, is that the variation is an effect of the solar wind. Another theory is that the variation is caused by the convective flows from the summer pole to the winter pole. The flows would descend at the winter pole, transporting heat to the cooler mesosphere from the higher altitudes. (Hess, 1968, p. 103)

d. Long Term Variations

It was found that there was a long-term density variation associated with the 11 year solar cycle. Measurements of the solar flux, or F10.7, taken over several years provide evidence of this effect. As can be seen in Figure 6 (Larson, 1992, p. 209), the sun has an 11 year cycle with maximum and minimum values of F10.7. The F10.7 measurement, explained in detail later, is a measurement of the EUV radiation. During periods of high solar activity, the solar flux is high, thus causing an increase in atmospheric density due to EUV heating and the resultant expansion. As can be assumed from the figure, the density of the upper atmosphere has a corresponding eleven year minimum and maximum.

B. THERMOSPHERIC PROCESSES

The upper atmosphere or thermosphere undergoes a change in composition and density due to several external inputs. The majority of the change is caused in response to the activity of the sun. The radiation from the sun, both thermal and ultraviolet, cause varying rates of change in the composition and hence the density of the atmosphere. The sun also causes changes in density due to the solar wind. The impingement of the solar material upon the earth's magnetosphere and upper atmosphere causes several changes in the make-up of the thermosphere and subsequently the overall density at altitude. The other major contributor to density variation of the earth's atmosphere is geomagnetic activity. Geomagnetic storms, although short-lived, cause a significant change in the atmospheric composition and density.

1. Solar EUV Radiation Effects

The first source of density change that will be addressed is the Extreme Ultraviolet Radiation produced by the sun. The sun's EUV radiation is the main cause of density variation in the earth's thermosphere. The solar EUV radiation is deposited mainly at low latitudes in the summer hemisphere. (Marcos, 1993, p. 2) The circulation and structure of the thermosphere at the low and middle latitudes are controlled by the heating caused by the absorption of the EUV radiation by the ozone layer in the lower thermosphere. The longer wavelength UV and visible radiation reach the lower atmosphere and hence heat the earth's surface. (Burns, 1991, p. 3) Most of the EUV radiation reaching the earth's atmosphere is absorbed at the 300 km level and the energy enters the atmosphere through photoionization. The energy that has been absorbed by the electrons and ions is passed to the neutral atmosphere by collisional processes. (Burns, 1991, p.3)

9

The solar EUV radiation also imparts a momentum to the neutral gas by the creation of pressure gradient forces that drive the neutral winds from the day to night regions and from the summer to winter hemisphere. (Burns, 1991, p. 3) Variations in the strength of the EUV radiation interacting with the thermosphere lead to changes in the composition and density of the neutral atmosphere. During the period of solar minimum, the EUV radiation produced by the sun is much less than that being produced during solar maximum. Therefore, the thermospheric temperatures and neutral densities will be low during a solar minimum than during solar max. This fact is illustrated in Figure 7. (Lars 1992, p. 209) It can be seen from this figure that the variation in density becomes much greater at higher altitudes during periods of high solar activity versus low solar activity.

Due to the fact that the solar EUV radiation is absorbed by the thermosphere, it makes it difficult to obtain a measurement of the EUV impinging on the atmosphere. This problem was solved by Jacchia in the early sixties. Jacchia discovered that the intensity found at 10.7cm closely corresponded to the amount of solar activity being witnessed. Currently the accepted measurement of solar flux is the F10.7 index. As can be seen in Figures 6 and 7, the typical value for F10.7 during solar minimum is 75, and has reached as high as 290 during the solar maximum period of 1958. A change in solar activity of this proportion would mean a change in density by a couple orders of magnitude at the altitude regime of interest.

One of the drawbacks of using F10.7 as a gauge of EUV radiation, is the fact that it lies at the other end of the spectrum from the EUV radiation, and is not a direct measure of the amount of EUV radiation reaching the thermosphere. Figure 8 (Hess, 1968, p. 668) illustrates the solar spectrum. It can be seen that the EUV radiation is at a frequency on the left hand side of the peak spectrum, whereas the solar flux measurement, F10.7, is on the right. Because the F10.7 index is not a direct measurement of the amount

of solar EUV radiation entering the atmosphere, accurate density calculations based on solar activity have some inherent error. Several programs have been initiated in order to remedy this problem, but currently the F10.7 index is the best indicator of solar flux available, and consequently is the index most widely used in atmospheric modeling.

2. Solar Wind

Another of the driving forces causing composition and density variation in the thermosphere is the solar wind. The solar wind consists of protons and electrons flowing outward from the sun's corona. Higher density plasma streams are also ejected from the sun during periods of flare and sunspot activity. (Fleagle, 1963, p. 236) The solar wind blows the interplanetary magnetic field lines across the polar cap in a direction away from the sun. (Burns, 1991, p. 4) This in turn causes a potential drop across the earth's magnetic polar cap as the interplanetary magnetic field encounters the earth's magnetic field. Field-aligned currents flow down to the ionosphere, closing the circuit, and producing an ion-convection pattern at high latitudes. The ions in this convection pattern collide with the neutral particles, driving them in a similar convection pattern. (Burns, 1991, p. 4) These collisions produce heat, which in turn produces a rising motion around the auroral zone. The up welling and the convection-driven neutral winds produce a composition and density change which spreads from the high latitudes to the lower latitudes.

The convection driven neutral winds also produce another significant heat source. Joule heating results from the frictional heating of the plasma as it is dragged through the neutral upper atmosphere by the auroral electric field forces. (Marcos, 1993, p. 3) This Joule heating is a substantial heat source, but becomes even more prevalent during periods of solar flare activity. Flares on the sun cause the solar wind to accelerate, driving the interplanetary magnetic field faster across the earth's magnetic field. This

increases the cross-cap potential and the rate of particle precipitation, and can also produce a magnetic substorm. (Burns, 1991, p. 5)

3. Geomagnetic Storms

Another of the major contributors of composition and density variation are geomagnetic storms. Geomagnetic storms are produced by the interaction of the interplanetary magnetic field with the earth's magnetic field. When solar flare activity is occurring, shock waves in the interplanetary magnetic field are driven into the earth's magnetic field causing rapid transients in the earth's magnetic field. This effect is monitored by means of the Ap index, or geomagnetic activity index, during periods of solar flare activity. The geomagnetic storm presents itself as a world-wide transient variation in the earth's magnetic field. The onset, or sudden commencement, of a magnetic storm is characterized by a rapid increase in the Ap index. Approximately 20 minutes later, the temperature and density of the auroral zones begins to increase.

One of the manifestations of geomagnetic storms is the generation of waves that propagate from the auroral regions to the lower latitudes. These waves take approximately eight hours to reach the lower latitudes. (Alder, 1992, p. 18) A typical magnetic storm, illustrated in Figure 9 (Akasofu, 1972, p. 557), lasts from 24 to 48 hours or longer. The effects of the geomagnetic storm on the density, last even longer and are quite pronounced at the higher altitudes. This is illustrated in Figure 10. (Ratcliffe, 1972, p. 35) It can be seen from Figure 10, that during periods of geomagnetic storms, the density at the altitude regime of interest increases several fold. This fact coupled with intense bombardment of EUV radiation, increases the density by several orders of magnitude.

4. Gravity Waves, Planetary Waves, and Tides

The final source of composition and density variation to be discussed are propagating tides and gravity waves. Atmospheric tides are caused primarily by the absorption of ultra-violet radiation by the ozone in the stratosphere, while gravity waves are caused by a variety of mechanisms which occur in the troposphere. A couple of these mechanisms are the shears associated with cold fronts and winds blowing over mountains. (Burns, 1991, p. 3) At lower altitudes, the semi-diurnal tide is the major contributor to density variation. This effect becomes less apparent at higher altitudes due to the fact that the semi-diurnal tide is dissipated by viscosity and ion drag. At higher altitudes, the diurnal tide becomes the driver of density variation and is caused by the absorption of the EUV radiation in the thermosphere. Overall, these waves and tides propagate up from the lower altitudes affecting the composition and density of the upper altitudes.

As a consequence of the above mentioned thermospheric processes, it is known that the temperature and hence the density of the upper atmosphere vary with the following parameters:

- solar flux (solar cycle and daily component)
- geomagnetic activity
- local time
- day of the year
- latitude
- longitude
- wave structures

C. PROGRAM DEVELOPMENT

The propagation program created for the atmospheric model comparison is a FORTRAN based program which uses a Runge-Kutta integrator. The propagator uses a form of Cowell's Method of orbital prediction. The program uses the position and velocity vectors in Cartesian coordinates as its inputs, and integrates over a designated time frame to produce the position and velocity vectors, also in Cartesian coordinates. Cowell's Method of orbital prediction has been found to be inaccurate due to the build-up of round off error. A more accurate method would have been to convert the Cartesian coordinates into normalized spherical coordinates in order to minimize the integration error build-up. Further research into this conversion is being conducted in order to obtain greater accuracy. For the purpose of the comparison, however, the accuracy of the result was not in question, but the accuracy of the atmospheric model, and its relative ease of use.

The propagation program consists of a series of subroutines which calculate the perturbing forces acting on the satellite. These forces, in the form of accelerations, are applied to the satellite's motion resulting in a position and velocity vector reflecting the result of the perturbing forces. Figure 11 and Table 1(Milani, 1987, p. 14-15) illustrate the various perturbing accelerations and their relative magnitude as a function of altitude. In order to obtain an accurate reflection of orbital motion at the altitude band in question, it was decided that in addition to the drag force, the earth's geopotential and third body attractions would also be included as perturbing forces.

1. Earth's Geopotential

As can be seen from Figure 11, the main perturbing force encountered by low earth orbiting satellites is the earth's gravity field. If the earth was a perfectly round and

smooth planet, then the forces of gravity could easily be modeled by the inverse square gravity law shown in equation 7.

$$\mathbf{g} = -\frac{\mu}{r^3}\mathbf{r} \tag{7}$$

However, since the earth is not perfectly spherical, and not smooth, the gravity field must be derived by obtaining the solution to Laplace's equation:

$$v^2V = 0 \tag{8}$$

where

$$V = G \int_{volume} \frac{dm}{\delta} \tag{9}$$

δ being the distance from the satellite to an incremental mass, dm, inside the earth, and G is the factor of proportionality in Newton's Law of Gravitation. Laplace then derived the basic equation for the geopotential shown below:

$$V = \frac{G}{r} \int \sum_{n=0}^{\infty} P_n(\cos\theta)\left(\frac{\rho}{r}\right)^n dm \tag{10}$$

By converting to spherical coordinates and applying Rodriguez' formula, the earth's geopotential takes the form of equation 11.

$$V = \frac{GM}{r}\left[1 + \sum_{n=2}^{\infty}\sum_{m=0}^{\infty}\left(\frac{a}{r}\right)^n P_{nm}(\sin\phi')(C_{nm}\cos m\lambda + \sin m\lambda)\right] \tag{11}$$

In this equation, V is the gravitational potential function, GM is the earth's gravitational constant, r is the radius vector from the earth's center of mass, a is the semi-major axis of the model ellipsoid, n and m designate the degree and order of the coefficients, ϕ is the geocentric latitude, λ is the geocentric longitude, C_{nm} and S_{nm} are the harmonic coefficients, and P_{nm} are the associated Legendre functions. (Ross, 1993, p.5-3) Several Earth gravitational models are currently in use in both the civilian and DoD communities.

The DoD currently uses the WGS-84 geopotential model as its gravitational model. The WGS-84 Earth gravitational model (EGM) contains a 180 by 180 matrix of zonal and tesseral harmonic coefficients. The WGS-84 EGM is currently being used for several DoD satellite programs including the GPS satellite constellation, and is considered to be an extremely accurate representation of the earth's geopotential. For most cases, the full matrix is not needed, and the matrix is truncated down to a 41 by 41 matrix. The truncated matrix provides an ample representation.

Currently, the propagation program contains the first 8 sets of zonal and tesseral coefficients. Future iterations of the propagation program will contain the complete 41 by 41 matrix. At the moment, attempts at configuring the propagation program in the WGS-84 coordinate system have failed. The first eight sets of coefficients vary only slightly from the first eight zonal terms of the more basic geopotential models and can be used without incurring significant errors during propagation.

2. Drag

For satellites in low earth orbit, drag is the other major perturbing force that must be modeled. Drag affects all satellites in all altitude regimes, but the affect is considered to be insignificant at altitudes greater than 1000 km. The following equation represents the atmospheric drag acceleration which is placed on an orbiting body.

$$a_D = \frac{1}{2} C_D \frac{A}{m} \rho V^2 \tag{12}$$

In this equation, a_D represents the drag acceleration imparted upon an orbiting satellite, C_D is the coefficient of drag, A is the cross sectional area of the satellite perpendicular to the direction of motion, m is the satellite mass, V is the satellite velocity and ρ is the local atmospheric density. The velocity used in this equation is computed by combining the geocentric velocity of the satellite with the contribution due to earth rotation and the wind

velocity at altitude. It is important to note that the wind component of the velocity cannot be ignored, and can be quite significant at altitudes in excess of 600 km. The neutral wind is a consequence of the activity caused by a geomagnetic disturbance. The change in drag can be 5% for every 200m/s of wind velocity. During a period of intense geomagnetic activity, the neutral winds can reach velocities in excess of 1 km/s which is equivalent to a 25% change in density. (Marcos, 1993, p. 6) In order to model this behavior, several atmospheric wind models have been developed. Models of the neutral winds begin with the efforts of Sissenwine in the late sixties, to the Horizontal Wind Model 90 (HWM 90). Currently these wind models are not incorporated into the empirical atmospheric drag models, but are incorporated in the general circulation models.

The coefficient of drag, C_D, is a difficult quantity to obtain. In order to determine the coefficient of drag, it must be determined whether the satellite is in a continuum flow, or a free molecular flow. This is done by determining the Knudsen number. The Knudsen number is the ratio between a typical dimension of the satellite and the average mean-free-path of the molecules found in the local atmosphere. When the Knudsen number is much less than one, the satellite is considered to be in a continuum flow. The satellite is considered to be in a free molecular flow when the Knudsen number is greater than one. Since the atmospheric density is so low at orbital altitudes, satellites in the upper atmosphere are characterized by free-molecular-flow aerodynamics. (Ross, 1994, p.16)

The collision of the atmospheric particles with the spacecraft produce the atmospheric drag force. The collisions can be classified under three categories: (1) elastic or specular reflection, (2) diffuse reflection and (3) absorption and subsequent emission. In elastic or specular reflection, the molecule collides with the satellite and is reflected away without transferring energy to the satellite. In diffuse reflection, the molecule

17

collides with the satellite and transfers a portion of its energy. Energy is also transferred to the satellite when molecules are absorbed on impact and later emitted. Since the satellite is considered to be in a free-molecular-flow, the coefficient of drag is obtained from a statistical mechanical calculation. (Ross, 1994, p. 16) Depending on the size and makeup of the satellite, the coefficient of drag can vary from 2.0 to 6.0. Table 2 (Larson, 1992, p. 207) illustrates the variation of the drag coefficient for various orbiting platforms. If the coefficient of drag cannot be determined, a value of 2.2 is used. For the purpose of this thesis, the coefficient of drag will remain constant at a value of 2.2.

In equation 12, the coefficient of drag, the cross sectional area, and the mass of the satellite all make up what is called the B-factor.

$$B = \frac{C_D A}{m} \qquad (13)$$

Inverting equation 13 will result in what is more widely known as the Ballistic coefficient. Current practice is to guess what the correct B-factor is for that given day and adjust the B-factor until the correct position and velocity is achieved. This does not seem to be orbital prediction, but rather orbital correction. If the size and shape of the satellite are known, as well as the mass, then the B-factor should only vary with varying coefficients of drag. However, most of the current orbital prediction schemes use the B-factor as a catch-all for any other errors in the modeling program. Hence the value of the B-factor is nowhere near the actual value. In this comparison, it was decided to keep the B-factor at a constant value in order to obtain a more accurate comparison between atmospheric models. It must be noted at this point that keeping the B-factor at its actual value is a major change, vice using the B-factor as an error catch-all.

The density for the drag acceleration calculations is of course derived from the atmospheric models. In the calculation of the drag acceleration, the density is the most

difficult to obtain, and frequently the one parameter with the greatest error. As a rule, the most current atmospheric models have a 15 to 20% inaccuracy rate, with this inaccuracy increasing as altitude increases. Due to this inaccuracy, the propagation scheme is only as accurate as the atmospheric model being used.

3. Third Body Attractions

The last of the perturbing forces currently included in the propagation program is that of third body attractions. In the case of the satellite program in question, the perturbing bodies are the sun and moon. As can be seen in Figure 11, both the sun and the moon contribute some small portion of disturbance force to a medium altitude satellite. In practice, this disturbance force is usually ignored for the low earth orbiting platforms, but in the altitude band in question (600 - 800km), these disturbance forces must not be ignored if a truly accurate representation of orbital motion is to be modeled. The equation used to find the perturbing acceleration due to the moon is described by equation 14 below.

$$\dot{\mathbf{v}} = -\frac{\mu}{r^3}\mathbf{r} - \mu_m\left(\frac{r_{ms}}{r_{ms}^3} - \frac{r_{m\oplus}}{r_{m\oplus}^3}\right) \tag{14}$$

In this equation, r is the radius from the earth to the satellite, r_{ms} is the radius from the moon to the satellite, $r_{m\oplus}$ is the radius from the earth to the moon, and μ_m is the gravitational parameter of the moon. (Bate, 1971, p. 389)

Currently the propagation scheme does not contain several perturbations that are important for accuracy purposes. At the moment, the sun's radiation pressure is ignored as well as the earth's albedo effect. Also, relativistic effects are ignored, which must eventually be incorporated in order to improve accuracy.

19

D. ATMOSPHERIC MODEL DEVELOPMENT

As mentioned previously, atmospheric models can be divided into two categories, the empirical models, and the general circulation models. The general circulation models are dynamic representations of the earth's atmosphere, and require extensive computational time in order to model the atmosphere. The general circulation models that have been recently created require Cray computers to run simulations. Efforts are currently under way to convert these models to a more user friendly format, so that they may be used on smaller computers. The empirical models, however, are readily available, and take little computational time per simulation. One drawback is that the accuracy of the models is quite a bit less than that of the general circulation models.

The history of the empirical earth atmospheric models dates back to the efforts of L. G. Jacchia in the late fifties. Once the early satellites such as Sputnik and Pioneer had been launched, immediate drag analysis was performed, and atmospheric models developed based on this analysis. The early models were crude, and only represented the regions where the satellites were orbiting. Little was understood of the variability of the environment and the density fluctuations being encountered. As more satellites, and a greater understanding of the sun's interaction with the earth's atmosphere was obtained, the accuracy of the atmospheric models increased. Figure 12 illustrates the developmental history of the various earth atmospheric drag models. (Marcos, 1993, p. 20) The mathematical development of the Lockheed-Densel or Jacchia 60 model, the Jacchia 71, and the MSIS 86 earth atmospheric models are described below.

1. Lockheed Densel

The Lockheed Densel, or Jacchia 60 earth atmospheric model was the first model to be implemented into the prediction scheme. As can be seen from Figure 12, it was one of the earliest atmospheric models contrived, and hence its accuracy is in great question. The Lockheed Densel model is actually a combination of two atmospheric models; the ARDC 1959 density model for low altitudes (h < 76 nautical miles), and the Jacchia 60 density formulation for h ≥ 76 nautical miles. For the density below 76 nautical miles, the density is obtained from the ARDC 1959 model which contains a table of density values as a function of altitude. The discussion on obtaining the density below 76 nm will not be discussed in this paper. When the density at an altitude above 76 nm is desired, the Jacchia 60 formulation is used. The first requirement is to define the unit vector to the diurnal bulge using the solar position and the bulge lag angle. In order to accomplish this the solar longitude must be determined by the following equation,

$$\lambda = \left(2\pi d \middle/ 365.25\right) - 1.41 + 0.0335 \sin\left(2\pi d \middle/ 365.25\right) \qquad (15)$$

where d represents the number of days since December 31, 1957. The unit vector to the sun is obtained from the following series of equations:

$$\ell_s = \cos\lambda \qquad m_s = \sin\lambda \cos\varepsilon \qquad n_s = \sin\lambda \sin\varepsilon \qquad (16)$$

where ε is the obliquity of the ecliptic. (Lockheed, 1992, p. B-100)

The unit vector to the diurnal bulge is then calculated in true of date coordinates by the following matrix

$$U_B = C \begin{bmatrix} \ell. \cos\theta - m. \sin\theta \\ m. \cos\theta + \ell. \sin\theta \\ n. \end{bmatrix} \tag{17}$$

where C = J2000.0 to true to date transformation matrix, and θ = 0.55 radians which equals the bulge lag angle. Two options are available to the user when using the solar flux value of F10.7. The user may either specify a value, or one is calculated using the following formula,

$$F_{10.7} = 1.5 + .8 \cos\left(2\pi d \middle/ 4020\right) \tag{18}$$

where once gain d is the number of days since December 31, 1957. This equation allows an approximation of the F10.7 value on any given day over the 11-year solar cycle period. (Lockheed, 1992, p. B-103) The Jacchia 60 model divides the atmosphere into a series of three bands for density calculation. The first band is from 76 - 108 nautical miles. The equation used to calculate the density in this altitude band is given by

$$\rho(h) = (\rho)_{76}\left(\frac{76}{h}\right)^p\left[\left(\frac{108-h}{32}\right) + 0.85F_{10.7}\left(\frac{h-76}{32}\right)^{4/3}\right]$$

$$\times\left[1.0 + \left(\frac{h-76}{1224}\right)(1.0 + \cos\varphi)^3\right] \tag{19}$$

$p = 7.18$

$(\rho)_{76}$ = density from ARDC 1959 model at 76 nm

h = altitude in nm

$F_{10.7}$ = solar flux measurement

$\cos\varphi = \dfrac{\overline{R} \bullet \overline{U}_s}{R}$ $\qquad \overline{R}$ = SV true of date position vector

$\overline{U}_s$ = diurnal bulge vector (equation 17).

The second altitude band ranges from 108 - 378 nautical miles, and the density calculation is given by equation 20;

$$\rho(h) = \rho_*(h)0.85F_{10.7}\left[1.0 + 0.02375\left(e^{0.0102h} - 1.9\right)(1.0 + \cos\varphi)^3\right] \qquad (20)$$

where $\qquad \rho_*(h) = k\exp\left[\left(-b - ab + 6.363e^{-0.0048h}\right)\log_{e}10\right]$

$a = 0.00368$, $b = 15.738$, and k is the conversion factor from slugs to kg/km^3. The third and final altitude band that is calculated in the Jacchia 60 model lies between 378 and 1000 nautical miles. Equation 21 is used to calculate the density in this region.

$$\rho(h) = \left(0.00504\,F_{10.7}\Big/_{h^8}\right)\left[0.125(1.0 + \cos\varphi)^3\left(h^3 - 6.0\times10^6\right) + 6.0\times10^6\right]k \qquad (21)$$

In the Jacchia 60 model it is assumed that the density is zero when the altitude is above 1000 nautical miles.

a. Mathematical Basis

In order to provide a mathematical background for the above density equations, the partial derivative equations are illustrated below. The partial derivative of the calculated density with respect to position is described by equation 22;

$$\frac{\partial\rho(h)}{\partial\overline{R}} = k_1\frac{\partial\rho(h)}{\partial h}\bullet\frac{\partial h}{\partial\overline{R}} + \frac{\partial\rho(h)}{\partial\varphi}\bullet\frac{\partial\varphi}{\partial\overline{R}} \qquad (22)$$

where k_1 is the conversion factor between nautical miles and kilometers. The partial derivative of the altitude with respect to $\overline{R}$ is best estimated by the following equation,

$$h = R - \frac{R_e\sqrt{1-e^2}}{\sqrt{1-e^2\cos^2\phi'}} \qquad (23)$$

R = position vector magnitude $\qquad\qquad\qquad$ R_e = earth equatorial radius

e = earth eccentricity $\qquad\qquad$ ϕ' =geocentric latitude

The differentiation yields equation 24;

$$\frac{\partial h}{\partial \overline{R}} = \frac{\overline{R}^T}{R} - R \left[\frac{\sqrt{1-e^2}\, e^2 \cos\phi'}{\left(1-e^2 \cos^2 \phi'\right)^{\frac{3}{2}}} \right] \frac{\partial \cos\phi'}{\partial \overline{R}} \qquad (24)$$

where

$\cos\phi' = \dfrac{\sqrt{X^2+Y^2}}{R}$, $\quad$ and $\quad \dfrac{\partial \cos\phi'}{\partial \overline{R}} = \dfrac{1}{R^4 \cos\phi'}\left[XZ^2, YZ^2, -Z\left(X^2+Y^2\right)\right]$ and

X, Y, and Z represent the geocentric coordinates of the orbiting object. The partial of φ with respect to $\overline{R}$ is described by the following relationship,

$$\frac{\partial \varphi}{\partial \overline{R}} = \frac{1}{\sin\varphi}\left[\frac{\overline{R}\cdot \overline{U}_s}{R^3}\overline{R} - \frac{\overline{U}_s}{R}\right]^T \qquad (25)$$

The partial derivative of $\rho(h)$ with respect to h and the partial of $\rho(h)$ with respect to φ are different for each of the altitude bands. In the altitude band between 76 and 108 nautical miles, the partial derivative of $\rho(h)$ with respect to h and φ are given by the following equations:

$$\frac{\partial \rho(h)}{\partial h} = -\frac{p}{h}\rho^{(h)} - \frac{AC}{32}\left[1 - 1.133 F_{10.7}\left(\frac{h-76}{32}\right)^{\frac{3}{2}}\right]$$

$$+\frac{AB}{1224}\left[1+\cos\varphi\right]^3 \qquad (26)$$

where $\rho(h)$ is the density found from equation 19, $p = 7.18$, and the variables A, B, and C follow (Lockheed, 192, p. B-105):

$$A = (\rho)_{76}\left[\frac{76}{h}\right]^p \qquad\qquad B = \left[\left(\frac{108-h}{32}\right) + 0.85 F_{10.7}\left(\frac{h-76}{32}\right)^{4/3}\right]$$

$$C = \left[1.0 + \left(\frac{h-76}{1224}\right)(1 + \cos\varphi)^3\right]$$

$$\frac{\partial \rho(h)}{\partial \varphi} = -3AB\left(\frac{h-76}{1224}\right)(1 + \cos\varphi)^2 \sin\varphi \qquad (27)$$

For the altitude band between 108 and 378 nautical miles, these two equations take on this form;

$$\frac{\partial \rho(h)}{\partial h} = -\rho(h)[a + 0.0305424\exp(-0.0048h)]\ell n 10$$

$$+0.0002059125\rho_*(h)F_{10.7}[\exp(0.0102h)](1 + \cos\varphi)^3 \qquad (28)$$

$$\frac{\partial \rho(h)}{\partial \varphi} = -0.0605625\rho_*(h)F_{10.7}[\exp(0.0102h) - 1.9](1 + \cos\varphi)^2 \sin\varphi \qquad (29)$$

In the highest altitude band between 378 and 1000 nautical miles, the equation take on the form (Lockheed, 1992, p. B-106)

$$\frac{\partial \rho(h)}{\partial h} = -\frac{8\rho(h)}{h} + \frac{0.00189F_{10.7}}{h^6}[1 + \cos\varphi]^3 k \qquad (30)$$

$$\frac{\partial \rho(h)}{\partial \varphi} = -\frac{0.00189F_{10.7}}{h^8}\left[(1 + \cos\varphi)^2 \sin\varphi(h^3 - 6.0\times 10^6)\right]k \qquad (31)$$

These equations can be used to implement an atmosphere in an orbital prediction program, and in fact are currently used for that purpose. The Jacchia 60 density model was one of the first empirical models on the market. With the launching of numerous satellites throughout the recent years, Jacchia et. al. have been able to expand on their empirical model. As can be seen from figure 12, several Jacchia models have been developed, each model building on its predecessor.

2. Jacchia-Roberts 71

The next model to be discussed is the Jacchia-Roberts 71 atmospheric model.
The Jacchia-Roberts 71 atmospheric model takes into account both the solar and the
geomagnetic activity during the time in question. L. G. Jacchia defined two empirical
profiles to represent temperature as a function of altitude and exospheric temperature.
One profile was defined between the region of 90 to 125 kilometers, and the other above
125 kilometers. Jacchia then used these temperature functions in the appropriate
thermodynamic differential equations to obtain density as a function of altitude and
exospheric temperature. (Lockheed, 1992, p. B-81) The Jacchia model as it stood was
very cumbersome and required a great amount of data storage to hold the data required,
so C. E. Roberts provided a method for evaluating the Jacchia model analytically. This
lead to a faster and more manageable model. The following are the equations used in
determining the atmospheric density as derived in the Jacchia-Roberts 71 atmospheric
model.

The first step in the model is to calculate the nighttime minimum global
exospheric temperature for zero geomagnetic activity,

$$T_c = 379^\circ + 3^\circ.24\overline{F}_{10.7} + 1^\circ.3\left[F_{10.7} - \overline{F}_{10.7}\right] \qquad (32)$$

where $\overline{F}_{10.7} = 81$ day running average of the F10.7 centered on the day in question. $F_{10.7}$
= solar flux measurement as obtained from the solar observatory at Ottawa, Canada.
(Jacchia, 1970, p. 16)

The value of the nighttime minimum exospheric temperature is then used in
calculating the uncorrected exospheric temperature as follows,

26

$$T_1 = T_c\left\{1 + 0.3\left[\sin^{22}\theta + \left(\cos^{22}\eta - \sin^{22}\theta\right)\cos^{30}\frac{\tau}{2}\right]\right\} \quad (33)$$

where

$$\eta = \frac{1}{2}|\phi - \delta| \qquad \theta = \frac{1}{2}|\phi + \delta| \qquad \tau = H - 37°.0 + 6°.0\sin(H + 43°.0) ,$$

$-\pi < \tau < \pi$

δ = the sun's declination

ϕ = the geodetic latitude of the satellite in true of date coordinates (includes earth flattening)

$$H = 180°.0\left\{\frac{(S_1 X_2 - S_2 X_1)}{\pi|S_1 X_2 - S_2 X_1|}\cos^{-1}\left[\frac{S_1 X_1 + S_2 X_2}{\left(S_1^2 + S_2^2\right)^{1/2}\left(X_1^2 + X_2^2\right)^{1/2}}\right]\right\} \quad (34)$$

The X variables are the components of the unit position vector of the satellite in true of date (TOD) coordinates, and the S variables are the components of the unit vector to the sun in TOD coordinates. (Lockheed, 1992, p. B-83)

It has been found through analyzing the effect of geomagnetic activity on the atmosphere, that there is a lag of approximately 6 to 7 hours from a detection of a density change from the actual geomagnetic disturbance. In order to account for this lag, the value of Kp is obtained for a period of 6.7 hours prior to the integration time in question. It must be noted that the Kp value only exists at a three hour resolution. At this point the correction for the exospheric temperature is calculated using the following formulas,

$$\Delta T_\infty = 28°.0 Kp + 0°.03 e^{Kp} \qquad \text{(Z} \geq \text{200 kilometers)}$$

$$\Delta T_\infty = 14°.0 Kp + 0°.02 e^{Kp} \qquad \text{(Z} < \text{200 kilometers)} \qquad (35)$$

The corrected exospheric temperature is then

$$T_{\infty} = T_1 + \Delta T_{\infty}$$

and the inflection point temperature is given by the following formula (Jacchia, 1970, p. 21)

$$T_x = 371°.6673 + 0.518806 T_{\infty} - 294°.3505 e^{-0.0021622 T_{\infty}} \qquad (36)$$

These values for the temperatures and the satellite altitude are used in the calculation presented by Roberts for the atmospheric density. However, a number of corrections must be applied due to several atmospheric processes presented by Jacchia. These corrections will be presented before continuing with the Roberts calculations.

One of the corrections deals with the direct effect of geomagnetic activity on the density below 200 kilometers. This correction is calculated by the following relation,

$$(\Delta \log \rho)_G = 0.012 Kp + 1.2 \times 10^{-5} e^{Kp} \qquad (37)$$

The next correction deals with the semi-annual density variation. This correction is calculated from the following relations, where Z is the altitude in kilometers.

$$(\Delta \log \rho)_{SA} = f(Z)g(t) \qquad (38)$$

where

$$f(Z) = (5.876 \times 10^{-7} Z^{2.331} + 0.06328)e^{-0.002868 Z} \qquad (39)$$

$$g(t) = 0.02835 + [0.3817 + 0.17829 \sin(2\pi \tau_{SA} + 4.137)]\sin(4\pi \tau_{SA} + 4.259) \qquad (40)$$

$$\tau_{SA} = \phi + 0.09544 \left\{ \left[\frac{1}{2} + \frac{1}{2}\sin(2\pi\phi + 6.035) \right]^{1.65} - \frac{1}{2} \right\} \qquad (41)$$

$$\phi = \frac{JD_{1958}}{365.2422} \qquad (42)$$

where JD_{1958} is the number of Julian days since January 1, 1958. (Lockheed, 1992, p. B-84)

The next correction deals with the seasonal latitudinal variations in the lower thermosphere. Equation 43 represents the general density variation, whereas equation 44 represents the correction for Helium specifically.

$$(\Delta \log \rho)_{LT} = 0.014(Z - 90)e^{\left[-0.0013(Z-90)^2\right]} \sin(2\pi\phi + 1.72)\sin\phi|\sin\phi| \quad (43)$$

$$(\Delta \log \rho)_{He} = 0.65\left|\frac{\delta_s}{\varepsilon}\right|\left[\sin^3\left(\frac{\pi}{4} - \frac{\phi\delta_s}{2|\delta_s|}\right) - 0.35355\right] \quad (44)$$

where ε is the obliquity of the ecliptic. (Lockheed, 1992, p. B-84)

Below 125 kilometers, Roberts uses the same temperature profile as Jacchia,

$$T(Z) = T_x + \frac{d_1}{35^4}\sum_{n=0}^{4} C_n Z^n \quad (45)$$

where

$d_1 = T_x - T_o, \quad T_o = 183°.0K$ and the coefficients follow

$C_0 = -89284375.0 \qquad C_2 = -52687.5 km^{-2} \qquad C_4 = -0.8 km^{-4}$

$C_1 = 3542400.0 km^{-1} \qquad C_3 = 340.5 km^{-3} \qquad (46)$

where T_x is the inflection point temperature at 125 kilometers calculated by equation 36. Roberts then substituted the temperature profile obtained from equation 45 into the barometric differential equation and integrated by partial fractions to obtain the following expression. Equation 47 represents the density found in the altitude band between 90 and 100 kilometers. (Lockheed, 1992, p. B-85)

$$\rho_s(Z) = \frac{\rho_o T_o}{M_o}\left(\frac{M(Z)}{T(Z)}\right)F_1^k \exp(kF_2) \quad (47)$$

where the "o" indicates the conditions at 90 kilometers. The mean molecular weight is calculated by the following equation,

$$M(Z) = \sum_{n=0}^{6} A_n Z^n \qquad (48)$$

where

$$A_0 = -435093.363387 \qquad A_3 = 11.043387545 km^{-3}$$

$$A_1 = 28275.5646391 km^{-1} \qquad A_4 = -0.08958790995 km^{-4}$$

$$A_2 = -765.33466108 km^{-2} \qquad A_5 = 0.00038737586 km^{-5}$$

$$A_6 = -0.000000697444 km^{-6}$$

These constants give a value of the mean molecular weight at 90 kilometers of 28.82678 which is close to the sea level mean molecular weight of 28.960. (Lockheed, 1992, p. B-86) The density of the lower limit is assumed to be constant at $\rho_* = 3.46 \times 10^{-9}\ gm/cm^3$. The constant k in equation 47 is evaluated by the following formula

$$k = -\frac{35^4\, g R_a^{\,2}}{R d_1 C_4} \qquad (49)$$

where g is assumed to be $9.80665 m/sec^2$, the acceleration due to gravity at sea level. The functions F_1 and F_2 in equation 47 are determined from equations 50 and 51.

$$F_1 = \left(\frac{Z+R_a}{90+R_a}\right)^{P_1}\left(\frac{Z-r_1}{90-r_1}\right)^{P_2}\left(\frac{Z-r_2}{90-r_2}\right)^{P_3}\left(\frac{Z^2-2XZ+X^2+Y^2}{8100-180X+X^2+Y^2}\right)^{P_4} \qquad (50)$$

$$F_2 = (Z-90)\left[A_6 + \frac{p_5}{(Z+R_a)(90+R_a)}\right] + \frac{p_6}{Y}\tan^{-1}\left[\frac{Y(Z-90)}{Y^2+(Z-X)(90-X)}\right] \qquad (51)$$

The variables r_1 and r_2 are the two real roots and X and Y are the real and imaginary parts (Y>0), respectively, of the complex conjugate roots of the following quadratic,

$$P(Z) = \sum_{n=0}^{4} C_n' Z^n \qquad (52)$$

with the following coefficients

$$C_0^* = \frac{35^4 T_X}{C_4 d_1} + \frac{C_0}{C_4} \quad \text{and} \quad C_n^* = \frac{C_n}{C_4} \quad 1 \le n \le 4$$

for values of C_n used in equation 45. The parameters p_i in equations 50 and 51 are

evaluated by the following relations (Lockheed, 1992, p. B-86)

$$p_2 = \frac{S(r_1)}{U(r_1)} \qquad p_3 = \frac{-S(r_2)}{U(r_2)} \qquad p_5 = \frac{S(-R_a)}{V}$$

$$p_4 = \left\{ B_0 - r_1 r_2 R_a^2 \left[B_4 + B_5 (2X + r_1 + r_2 - R_a) \right] + W(r_1) p_2 \right\} / X^*$$

$$- \left\{ r_1 r_2 B_5 R_a (X^2 + Y^2) + W(r_2) p_3 + r_1 r_2 (R_a^2 - X^2 - Y^2) p_5 \right\} / X^*$$

$$p_6 = B_4 + B_5 (2X + r_1 + r_2 - R_a) - p_5 - 2(X + R_a) p_4 - (r_2 + R_a) p_3 - (r_1 + R_a) p_2$$

$$p_1 = B_5 - 2 p_4 - p_3 - p_2$$

where

$$X^* = -2 r_1 r_2 R_a (R_a^2 + 2XR_a + X^2 + Y^2)$$

$$V = (R_a + r_1)(R_a + r_2)(R_a^2 + 2XR_a + X^2 + Y^2)$$

$$U(r_i) = (r_i + R_a)^2 (r_i^2 - 2Xr_i + X^2 + Y^2)(r_1 - r_2)$$

$$W(r_i) = r_1 r_2 R_a (R_a + r_i) \left(R_a + \frac{X^2 + Y^2}{r_i} \right)$$

and

$$B_n = \alpha_n + \beta_n \frac{T_X}{T_X - T_0} \qquad (n = 0, 1, \dots 5)$$

$$S(Z) = \sum_{n=0}^{5} B_n Z^n$$

with the coefficients

$\alpha_0 = 3144902516.672729$ $\qquad\qquad$ $\beta_0 = -52864482.17910969$

$\alpha_1 = -123774885.4832917$ $\qquad\qquad$ $\beta_1 = -16632.50847336828$

$$\alpha_2 = 1816141.096520398 \qquad\qquad \beta_2 = -1.308252378125$$

$$\alpha_3 = -11403.31079489267 \qquad\qquad \beta_3 = 0.0$$

$$\alpha_4 = 24.36498612105595 \qquad\qquad \beta_4 = 0.0$$

$$\alpha_5 = 0.008957502869707995 \qquad\qquad \beta_5 = 0.0$$

Equation 47 is a valid equation below 100 kilometers where mixing is assumed to be predominant. However, above 100 kilometers, diffusive equilibrium is assumed, and it is necessary to substitute the profile given by equation 45 into the diffusion differential equation (one for each constituent of the atmosphere), and integrated by partial fractions. This was done by Roberts to yield the density for the altitude band between 100 and 125 kilometers, given by equation 52.

$$\rho_s(Z) = \sum_{i=1}^{5} \rho_i(Z) \qquad\qquad (52)$$

It is computationally expensive to calculate the density at 100 kilometers at different exospheric temperatures by using equation 47. Thus values for the density at 100 km were pre computed at several values of the exospheric temperature, and these values could then be extracted instead of using valuable computer time and memory. Next the atmospheric constituent mass densities are calculated by the following,

$$\rho_i(Z) = \rho(100)\frac{M_i}{M_s}\mu_i\left[\frac{T(100)}{T(Z)}\right]^{1+\alpha_i} F_3^{M_i k} \exp(M_i k F_4) \qquad (53)$$

The index i corresponds to the values 1 through 6 of the various atmospheric constituents of N_2, Ar, He, O_2, O, and H, respectively. The constants found in equation 53 are the characteristics of these species and are tabulated in Table 3 of Lockheed 1992. Hydrogen is not a significant constituent below 125 kilometers, so it is not included in the

calculations. (Lockheed, 1992, p. B-89) The temperature at 100 kilometers is calculated from the following,

$$T(100) = T_X + \Omega d_1 \quad \text{where} \quad \Omega = 35^{-4} \sum_{n=0}^{4} C_n (100)^n = -0.94585589 \quad (54)$$

and F_3 and F_4 are calculated by equations 55 and 56

$$F_3 = \left(\frac{Z + R_a}{R_a + 100} \right)^{q_1} \left(\frac{Z - r_1}{100 - r_1} \right)^{q_2} \left(\frac{Z - r_2}{100 - r_2} \right)^{q_3} \left(\frac{Z^2 - 2XZ + X^2 + Y^2}{100^2 - 200X + X^2 + Y^2} \right)^{q_4} \quad (55)$$

$$F_4 = \frac{q_5 (Z - 100)}{(Z + R_a)(R_a + 100)} + \frac{q_6}{Y} \tan^{-1} \left[\frac{Y(Z - 100)}{Y^2 + (Z - X)(100 - X)} \right] \quad (56)$$

where the parameters q_i are calculated by

$$q_2 = \frac{1}{U(r_1)}$$

$$q_3 = \frac{-1}{U(r_2)}$$

$$q_5 = \frac{1}{V}$$

$$q_4 = \left\{ 1 + r_1 r_2 \left(R_a^2 - X^2 - Y^2 \right) q_5 + W(r_1) q_2 + W(r_2) q_3 \right\} / X^*$$

$$q_6 = -q_5 - 2(X + R_a) q_4 - (r_2 + R_a) q_3 - (r_1 + R_a) q_2$$

$$q_1 = -2q_4 - q_3 - q_2$$

All of the variables in these equations have been defined earlier.

For the region above 125 kilometers, it is still a valid assumption that diffusive equilibrium is dominant, but the temperature given by equation 45 is no longer valid. Jacchia defined the temperature profile of the upper altitude regions by the following empirical asymptotic function:

$$T(Z) = T_x + \frac{2}{\pi}(T_\infty - T_x)\tan^{-1}\left\{0.95\pi\left(\frac{T_x - T_0}{T_\infty - T_x}\right)\left(\frac{Z - 125}{35}\right)\left[1 + 4.5\times10^{-6}(Z - 125)^{2.5}\right]\right\} \quad (57)$$

In order to integrate the diffusion differential equations in closed form, Roberts replaced equation 57 with the following (Lockheed. 1992, p. B-90)

$$T(Z) = T_\infty - (T_\infty - T_x)\exp\left[-\left(\frac{T_x - T_0}{T_\infty - T_x}\right)\left(\frac{Z - 125}{35}\right)\left(\frac{\ell}{R_a + Z}\right)\right] \quad (58)$$

The parameter ℓ will be discussed later.

Integration of equation 58 yields the following equation, which is valid for all of the constituents except hydrogen.

$$\rho_i(Z) = \rho_i(125)\left(\frac{T_x}{T}\right)^{1+\alpha_i+\gamma_i}\left(\frac{T_\infty - T}{T_\infty - T_x}\right)^{\gamma_i} \quad (59)$$

where

$$\gamma_i = \frac{M_i g R_a^2}{R\ell T_\infty}\left(\frac{T_\infty - T_x}{T_x - T_0}\right)\left(\frac{35}{6481.766}\right) \quad (60)$$

At this point several corrections are made for the particular constituent densities due to seasonal changes. The value of the helium density that is calculated by using equation 59, must be corrected due to the seasonal latitudinal variation as given by equation 44. The specific form is presented below

$$\left[\rho_3(Z)\right]_{corrected} = \rho_3(Z)10^{(\Delta\log\rho)_{He}} \quad (61)$$

where i corresponds to the index of helium presented above. Above 500 kilometers, the concentration becomes significant, therefore it must be accounted for by the following

$$\rho_6(Z) = \rho_6(500)\left[\frac{T(500)}{T(Z)}\right]^{1+\alpha_6+\gamma_6}\left[\frac{T_\infty - T(Z)}{T_\infty - T(500)}\right]^{\gamma_6} \quad (62)$$

where the hydrogen density at 500 kilometers can be calculated from

34

$$\rho_6(500) = \frac{M_6}{A} 10^{[73.13-(39.4-5.5\log T_{500})\log T_{500}]} \tag{63}$$

The temperature at 500 kilometers is calculated by using equation 58. The constituents are summed and the standard density above 125 kilometers is given by the following (Lockheed, 1992, p. B-94):

$$\rho_s(Z) = \sum_{i=1}^{6} \rho_i(Z) \tag{64}$$

So far, the standard atmospheric density at any given altitude has been calculated, but the densities calculated using equations 47, 52, or 64 must now be corrected for geomagnetic activity, the semi-annual variation and the seasonal latitudinal variation by equations 37, 38, and 43 respectively. The effects of these variations can be summed logarithmically to obtain the following relation

$$(\Delta \log \rho)_{corr} = (\Delta \log \rho)_G + (\Delta \log \rho)_{SA} + (\Delta \log \rho)_{LT} \tag{65}$$

The final corrected density at any altitude can then be determined by

$$\rho(Z) = \rho_s 10^{(\Delta \log \rho)_{corr}} \tag{66}$$

Due to the introduction of equation 58 in the place of Jacchia's equation (57) for temperature, the results of the Roberts portion of the model did not exactly concur with those that were observed by Jacchia. This effect was only in the upper portion of the model, whereas the lower altitude bands agreed exactly(as should be the case). This is where the ℓ parameter comes into play in equation 58. Values of the ℓ parameter were calculated in order to obtain the best least squares fit of density versus altitude (125 - 2500km) to the Jacchia tabulated data. The maximum deviation from the Jacchia density values is less that 6.7%. (Lockheed, 1992, p. B-94) The derivation and values of the parameter ℓ can be found in the Lockheed reference, and will not be discussed in this paper.

a. Mathematical Basis

The following section contains the partial derivatives of the Jacchia-Roberts model. Starting from equation 66, the partial derivative of density with respect to local position can be found. This can then be used in orbital prediction schemes in order to better model the satellite's orbital trajectory. The following equation is a simple restatement of equation 66.

$$\rho(Z) = \rho_s(Z)\Delta\rho_{corr} \qquad (67)$$

The desired partial derivative then becomes

$$\frac{\partial\rho}{\partial\overline{R}} = \rho_s \frac{\partial(\Delta\rho_c)}{\partial\overline{R}} + \Delta\rho_c \frac{\partial\rho_s}{\partial\overline{R}} \qquad (68)$$

The variation of the correction factor with respect to the satellite position is derived from equations 65 and 37 through 43.

$$\frac{\partial(\Delta\rho_c)}{\partial\overline{R}} = \frac{\Delta\rho_c}{0.4342944819}\left\{ g(t)f'(Z)\frac{\partial Z}{\overline{R}} + 0.14\sin(2\pi\phi + 1.72)e^{-0.0013(Z-90)^2} \right.$$

$$\left. \times\left[\left(1 - 0.0026\{(Z-90)\}^2\right)\sin\phi|\sin\phi|\frac{\partial Z}{\partial\overline{R}} + 2(Z-90)|\sin\phi|\cos\phi\frac{\partial\phi}{\partial\overline{R}} \right] \right\} \qquad (69)$$

where

$$f'(Z) = -0.002868f(Z) + 2.331(5.876\times10^{-7})Z^{1.331}e^{-0.002868 Z} \qquad (70)$$

The variation of altitude with respect to position, $\partial Z/\partial\overline{R}$, is the same as that calculated in equation 24. The variation of geodetic latitude with respect to position is derived by differentiating the following equation

$$\phi = \tan^{-1}\left\{ \frac{1}{(1-f)^2}\left[\frac{X_3}{(X_1^2 + X_2^2)^{1/2}} \right] \right\} \qquad (71)$$

to obtain

$$\frac{\partial \phi}{\partial \overline{R}} = \frac{\sin 2\phi}{2} \begin{bmatrix} \dfrac{-X_1}{X_1^2 + X_2^2} \\ -\dfrac{X_2}{X_1^2 + X_2^2} \\ \dfrac{1}{X_3} \end{bmatrix}^T \qquad (72)$$

The variation of standard density with respect to position is calculated directly from the barometric differential equation for altitudes below 100 kilometers

$$\frac{\partial \rho_S}{\partial \overline{R}} = \rho_S \left\{ \left[\frac{1}{M} \sum_{n=1}^{6} nA_n Z^{n-1} - \frac{Mg}{RT} \right] \frac{\partial Z}{\partial \overline{R}} - \frac{1}{T} \frac{\partial T}{\partial \overline{R}} \right\} \qquad (73)$$

and from the diffusion differential equation above 100 kilometers

$$\frac{\partial \rho_S}{\partial \overline{R}} = -\frac{1}{T} \left\{ \left[\frac{\rho' g_0 R_a^2}{R(Z+R_a)^2} \right] \frac{\partial Z}{\partial \overline{R}} + (\rho_S + \alpha_3 \rho_3) \frac{\partial T}{\partial \overline{R}} \right\} \qquad (74)$$

where

$$\rho' = \sum_{i=1}^{6} \rho_i M_i \qquad (75)$$

The partial derivatives of the temperature with respect to position are derived by differentiating equation 45 for altitudes less than 125 kilometers

$$\frac{\partial T}{\partial \overline{R}} = \frac{T - T_0}{d_1} \left(\frac{\partial T_X}{\partial T_\infty} \frac{\partial T_\infty}{\partial \overline{R}} \right) + \left(\frac{d_1}{35^4} \sum_{n=1}^{4} nC_n Z^{n-1} \right) \frac{\partial Z}{\partial \overline{R}} \qquad (76)$$

or equation 58 for altitudes above 125 kilometers

$$\frac{\partial T}{\partial \overline{R}} = \frac{\partial T_\infty}{\partial \overline{R}} + \left(\frac{T - T_\infty}{T_\infty - T_X} \right) \left\{ \left(1 - \frac{\partial T_X}{\partial T_\infty} \right) - \left(\frac{Z - Z_X}{R_a + Z} \right) \left(\frac{\ell}{35} \right) \right\}$$

$$\times \left[\frac{\partial T_{X}}{\partial T_{\infty}} - \frac{T_{X}-T_{0}}{T_{\infty}-T_{X}}\left(1-\frac{\partial T_{X}}{\partial T_{\infty}}\right) + \frac{T_{X}-T_{0}}{\ell}\sum_{j=1}^{4} j\ell_{j} T_{\infty}^{j-1} \right] \frac{\partial T_{\infty}}{\partial \overline{R}}$$

$$-\left(\frac{T-T_{\infty}}{T_{\infty}-T_{X}}\right)\left(T_{X}-T_{0}\right)\left[\frac{R_{a}+Z_{X}}{\left(R_{a}+Z\right)^{2}}\right]\left(\frac{\ell}{35}\right)\frac{\partial Z}{\partial R} \qquad (77)$$

and finally, the derivatives of T_{X} and T_{∞} with respect to position are derived by differentiating equations 36 and 33 respectively,

$$\frac{\partial T_{X}}{\partial T_{\infty}} = 0.0518806 + (294.3505)(0.0021622)e^{-0.0021622 T_{\infty}} \qquad (78)$$

$$\frac{\partial T_{\infty}}{\partial \overline{R}} = 0.3 T_{c}\left\{ 2.2 \sin^{1.2}\theta\cos\theta\left(1-\cos^{3.0}\frac{\tau}{2}\right)\frac{\partial \theta}{\partial \overline{R}} \right.$$

$$\left. -2.2\cos^{1.2}\eta\sin\eta\cos^{3.0}\frac{\tau}{2}\frac{\partial \eta}{\partial \overline{R}} - \frac{3}{2}\left(\cos^{2.2}\eta - \sin^{2.2}\theta\right)\cos^{2}\frac{\tau}{2}\sin\frac{\tau}{2}\frac{\partial \tau}{\partial \overline{R}} \right\} \qquad (79)$$

where

$$\frac{\partial \eta}{\partial \overline{R}} = \frac{1}{2}\frac{\phi - \delta_{s}}{|\phi - \delta_{s}|}\frac{\partial \phi}{\partial \overline{R}}$$

$$\frac{\partial \theta}{\partial \overline{R}} = \frac{1}{2}\frac{\phi + \delta_{s}}{|\phi + \delta_{s}|}\frac{\partial \phi}{\partial \overline{R}}$$

$$\frac{\partial \tau}{\partial X_{i}} = \frac{\pi}{180}\left\{1+\frac{\pi}{30}\cos\left[\frac{\pi(H+43.0)}{180}\right]\right\}\frac{\partial H}{\partial X_{i}} \qquad (i = 1,2)$$

$$\frac{\partial H}{\partial X_{i}} = \frac{180}{\pi}\left(\frac{(S_{1}X_{2}-S_{2}X_{1})}{|S_{1}X_{2}-S_{2}X_{1}|}\right)$$

$$\times \left\{\frac{1}{\left[(X_{1}^{2}+X_{2}^{2})(S_{1}^{2}+S_{2}^{2})-(S_{1}X_{1}+S_{2}X_{2})^{2}\right]1/2}\right\}\left[\frac{(S_{1}X_{1}-S_{2}X_{2})X_{i}}{X_{1}^{2}+X_{2}^{2}}-S_{i}\right] \qquad (i = 1,2)$$

$$\frac{\partial \tau}{\partial X_3} = 0$$

$$\frac{\partial H}{\partial X_3} = 0$$

3. MSIS 86 (Mass Spectrometer and Incoherent Scatter 86)

The Lockheed Densel model and the Jacchia 71 model, both developed by

Luigi Jacchia, use drag analysis data from earth orbiting satellites to derive the densities of

the various altitude bands associated within the models. A. E. Hedin chose a different

approach to the problem of modeling the atmosphere. Hedin's approach was to use actual

density data retrieved from orbiting instruments aboard several satellites and combine this

data with measurements taken by ground based incoherent scatter radar stations. Hedin,

et. al., began the original MSIS model using the total densities inferred from Jacchia's

models, however, it was found that the measurements of the temperature found by the

incoherent scatter method differed significantly. (Hedin, 1972, p. 2139) These differences

were noted in the time of daily maximum, and the amplitude of the daily and annual

variations of the density. Hedin used the data that was obtained from the mass

spectrometers on board several orbiting satellites to confirm this. The measurements from

the satellites as well as the ground based incoherent scatter measurements provide

information at different altitudes, latitudes, longitudes, solar activities , and seasons.

The MSIS 86 model is the culmination of years of research and development as

can be seen in figure 1. The formulation of the MSIS models is based on a spherical

harmonic expansion of exospheric temperature and effective lower boundary densities

which uses local solar time and geographic latitude as the independent variables. This expansion is a special case of a more general expansion based on longitude and latitude, where the coefficients of the expansion are represented by a Fourier series in universal time. (Hedin, 1979, p. 2)

This leads to the following expansion

$$\Delta G = \sum_{m=0}^{\infty}\sum_{l=0}^{\infty}\sum_{n=-l}^{l} P_{ln}\left[a_{ln}^{m}\cos(m\omega't+n\lambda)+b_{ln}^{m}\sin(m\omega't+n\lambda)\right] \quad (80)$$

where

P_{ln} = Legendres associated functions in geographic latitude

t = universal time in seconds

$\omega' = 2\pi/86400s^{-1}$

λ = geographic longitude in radians

This particular expansion was used for the initial MSIS models. With the launching of several more satellites equipped with mass spectrometers, and the addition of several more incoherent scatter radars, the model evolved into the MSIS83, and eventually the MSIS 86.

The main emphasis now is the formulation of the MSIS 86 model. Hedin explains that the models uses a Bates temperature profile as a function of geopotential height for the upper thermosphere, and an inverse polynomial in geopotential height for the lower thermosphere. (Hedin, 1987, p. 4649) The exospheric temperature and other key quantities are expressed as functions of geographical and solar/magnetic parameters. The temperature profiles allow for the exact integration of the hydrostatic equation for a constant mass to determine the density profile based on a density specified at 120 kilometers as a function of geographical latitude and solar/magnetic parameters. The MSIS 83 model used the expansion formula (Equation 80) to model the variations due to

local time, latitude, longitude, universal time, F10.7, and Ap. The MSIS 86 model enhances the MSIS 83 model by adding terms to express hemispherical and seasonal differences in the polar regions and local time variations in the magnetic activity effect.

The following equations are the complete formulation of the MSIS 86 atmospheric model. The first step in the formulation is to obtain an expression for the temperature profile.

$$T(Z) = T_\infty - (T_\infty - T_l)\exp^{[-\sigma\xi(Z.Z_l)]} \quad \text{where } Z \geq Z_a \tag{81}$$

$$T(Z) = 1/(1/T_0 + T_B x^2 + T_C x^4 + T_D x^6) \quad \text{where } Z < Z_a \tag{82}$$

the matching temperature and temperature gradient at Z_a equals

$$T_a = T(Z_a) = T_\infty - (T_\infty - T_l)\exp^{[-\sigma\xi(Z_a.Z_l)]} \tag{83}$$

$$T_a' = T'(Z_a) = (T_\infty - T_a)\sigma[(R_p + Z_l)/(R_p + Z_a)]^2 \tag{84}$$

$$T_D = 0.66666\xi(Z_0,Z_a)T_a'/T_a^2 - 3.11111(1/T_a - 1/T_0) + 7.11111(1/T_{12} - 1/T_0) \tag{85}$$

$$T_C = \xi(Z_0,Z_a)T_a'/(2T_a^2) - (1/T_a - 1/T_0) - 2T_D \tag{86}$$

$$T_B = (1/T_a - 1/T_0) - T_C - T_D \tag{87}$$

$$x = -[\xi(Z_a,Z) - \xi(Z_0,Z_a)]/\xi(Z_0,Z_a) \tag{88}$$

$$T_{12} = T_0 + T_R(T_a - T_0) \tag{89}$$

$$\xi(Z,Z_l) = (Z - Z_l)(R_p + Z_l)/(R_p + Z) \tag{90}$$

$$\xi(Z,Z_a) = (Z - Z_a)(R_p + Z_a)/(R_p + Z) \tag{91}$$

$$\sigma = T_l'/(T_\infty - T_l) \qquad\qquad T_l = \overline{T_l}[1 + G(L)]$$

$$T_l' = \overline{T_l}'[1 + G(L)] \qquad\qquad T_0 = \overline{T_0}[1 + G(L)]$$

$$T_\infty = \overline{T_\infty}[1 + G(L)] \qquad\qquad Z_0 = \overline{Z_0}[1 + G(L)]$$

$$T_R = \overline{T_R}[1 + G(L)]$$

where (all temperatures in Kelvin)

T = ambient temperature $\qquad\qquad$ $\overline{T_0}$ = average mesopause temperature

41

T_a = temperature at Z_a $\overline{T_l}'$ = average temperature gradient at Z_l

T_a' = temperature gradient at Z_a in K/km $\overline{T_R}$ = average mesopause shape factor

T_{12} = temperature at $(Z_0 + Z_l)/2$ Z = altitude in km

$\overline{T_\infty}$ = average exospheric temperature Z_l = 120 km

$\overline{T_l}$ = average temperature at Z_l

Z_a = altitude of temperature profile junction; 117.2 km

$\overline{Z_0}$ = average mesopause height R_p = 6356.77 km

Hedin now explains that the density profile is a combination of diffusive and mixing profiles multiplied by one or more factors $C_1...C_n$ to account for chemistry or the dynamics flow effects. (Hedin, 1987, p. 4638)

$$n(Z,M) = \left[n_d(Z,M)^A + n_m(Z,M)^A \right]^{1/A} \left[C_1(Z)...C_n(Z) \right] \quad (92)$$

$$A = M_h / \left(\overline{M_0} - M \right) \quad (93)$$

where

n = ambient density $M_h = 28$

n_d = diffusive profile $\overline{M_0} = 28.95$

n_m = mixing profile M = molecular weight of gas species

The Following equations represent the diffusive profile and the mixing profile. The diffusive profile is given by the following

$$n_d(Z,M) = n_l D(Z,M) \left[T(Z_l)/T(Z) \right]^{1+\alpha} \quad (94)$$

$$D(Z,M) = D_B(Z,M) \quad Z \geq Z_a \quad (95)$$

$$D(Z,M) = D_B(Z_a,M) \exp^{\left\{ T_l\left[(x-1)/T_0 + T_B(x^3-1)/3 + T_C(x^5-1)/5 + T_D(x^7-1)/7 \right] \right\}} \quad (Z < Z_a) \quad (96)$$

$$D_B(Z,M) = \left[T(Z_l)/T(Z) \right]^{\gamma_2} \exp^{\left[-\alpha \gamma_2 \xi(z,z_l) \right]} \quad (97)$$

42

$$\gamma_2 = Mg_l \big/ \big(\sigma R_g T_\infty \big) \qquad\qquad g_a = g_s \big/ \big(1 + Z_a / R_p \big)^2$$

$$\gamma_1 = Mg_a \xi(Z_0, Z_a) / R_g \qquad\qquad g_l = g_s \big/ \big(1 + Z_l / R_p \big)^2$$

$$n_l = \bar{n}_l \exp^{[G(L)]} \tag{98}$$

where

$\bar{n}_l$ = the average density at Z_l

$g_s = 9.80665 \times 10^{-3} \, km / s^2$

$R_g = 8.314 \times 10^{-3}$ g km^2/mols s^2 deg

and α is the thermal diffusion coefficient of -0.4 for He and zero for the rest of the

constituents.

The mixing profile is given by the following

$$n_m(Z, M) = n_l \big[D(Z_h, M) / D(Z_h, \bar{M}_0) \big] \big[T(Z_l) / T(Z_h) \big]^\alpha D(Z, \bar{M}_0) \big[T(Z_l) / T(Z) \big] \tag{99}$$

Hedin (1987), goes into a procedure to simulate the chemistry and dynamic flow

effects of the turbopause which provides a specified mixing ratio with respect to nitrogen.

$$C_1(Z) = \exp\left\{ R_1 \big/ \big[1 + \exp^{(Z - Z_1)/H_1} \big] \right\} \tag{100}$$

$$R_1 = \log\big[\Omega n_m(Z_l, 28) / n_m(Z_l, M) \big] \tag{101}$$

where Ω is the mixing ratio relative to N_2, Z_1 is the altitude at which $\log_{10} C_1$ is R/2,

and H_1 is the scale height for this correction. There is a peak in the mixing ratio in the

lower thermosphere due to O, N, and H. This peak is modeled by the following

$$C_2(Z) = \exp\left\{ R_2 \big/ \big[1 + \exp(Z - Z_2)/H_2 \big] \right\} \tag{102}$$

where R_2 is the density correction parameter, Z_2 is the altitude where $\log_{10}$ density

correction is $R_2/2$, and H_2 is the scale height of the correction. As mentioned above, the

MSIS 86 atmospheric model attempts to model all the known causes of the variations of density. This is done by the expansion function (Equation 80). The following is the expansion function for the MSIS 86 model quantities:

Time independent

$$G = a_{10}P_{10} + a_{20}P_{20} + a_{40}P_{40}$$

Solar activity

$$+F_{00}^{a1}\Delta\overline{F} + F_{00}^{a2}(\Delta\overline{F})^2 + f_{00}^{a1}\Delta F + f_{00}^{a2}(\Delta F)^2 + \overline{f}_{20}^{a1}P_{20}\Delta\overline{F}$$

Symmetrical annual

$$+c_{00}^1 \cos\Omega_d(t_d - t_{00}^{c1})$$

Symmetrical semiannual

$$+(c_{00}^2 + c_{20}^2 P_{20})\cos2\Omega_d(t_d - t_{00}^{c2})$$

Asymmetrical annual (seasonal)

$$+(c_{10}^1 P_{10} + c_{30}^1 P_{30})F_1 \cos2\Omega_d(t_d - t_{10}^{c1})$$

Asymmetrical semiannual

$$+c_{10}^2 P_{10} \cos2\Omega_d(t_d - t_{10}^{c2})$$

Diurnal

$$+\left[a_{11}P_{11} + a_{31}P_{31} + a_{51}P_{51} + c_{21}^1 P_{21} \cos\Omega_d(t_d - t_{10}^{c1})\right]F_2 \cos\omega\tau$$

$$+\left[b_{11}P_{11} + b_{31}P_{31} + b_{51}P_{51} + d_{21}^1 P_{21} \cos\Omega_d(t_d - t_{10}^{c1})\right]F_2 \sin\omega\tau$$

Semidiurnal

$$+\left[a_{22}P_{22} + a_{42}P_{42} + (c_{32}^1 P_{32} + c_{52}^1 P_{52})\cos\Omega_d(t_d - t_{10}^{c1})\right]F_2 \cos2\omega\tau$$

$$+\left[b_{22}P_{22} + b_{42}P_{42} + (d_{32}^1 P_{32} + d_{52}^1 P_{52})\cos\Omega_d(t_d - t_{10}^{c1})\right]F_2 \sin2\omega\tau$$

44

Terdiurnal

$$+\left[a_{33}P_{33}+\left(c_{43}^1 P_{43}+c_{63}^1 P_{63}\right)\cos\Omega_J\left(t_d-t_{10}^{c1}\right)\right]F_2\cos 3\omega\tau$$

$$+\left[b_{33}P_{33}+\left(d_{43}^1 P_{43}+d_{63}^1 P_{63}\right)\cos\Omega_d\left(t_d-t_{10}^{c1}\right)\right]F_2\sin 3\omega\tau$$

Magnetic activity

$$+\left[k_{00}^a+k_{20}^a P_{20}+k_{40}^a P_{40}+\left(k_{10}^{c1}P_{10}+k_{30}^{c1}P_{30}+k_{50}^{c1}P_{50}\right)\cos\Omega_J\left(t_d-t_{10}^{c1}\right)\right.$$

$$\left.+\left(k_{11}^a P_{11}+k_{31}^a P_{31}+k_{51}^a P_{51}\right)\cos\omega\left(\tau-t_{11}^k\right)\right]\Delta A$$

Longitudinal

$$+\left[a_{21}^0 P_{21}+a_{41}^0 P_{41}+a_{61}^0 P_{61}+a_{11}^0 P_{11}+a_{31}^0 P_{31}+a_{51}^0 P_{51}+\left(a_{11}^{c1}P_{11}+a_{31}^{c1}P_{31}\right)\cos\Omega_J\left(t_d-t_{10}^{c1}\right)\right]$$

$$\times\left(1+F_{21}^{a0}\Delta\overline{F}\right)\cos\lambda$$

$$+\left[b_{21}^0 P_{21}+b_{41}^0 P_{41}+b_{61}^0 P_{61}+b_{11}^0 P_{11}+b_{31}^0 P_{31}+b_{51}^0 P_{51}+\left(b_{11}^{c1}P_{11}+b_{31}^{c1}P_{31}\right)\cos\Omega_d\left(t_d-t_{10}^{c1}\right)\right]$$

$$\times\left(1+F_{21}^{a0}\Delta\overline{F}\right)\sin\lambda$$

UT

$$+\left(a_{10}^1 P_{10}+a_{30}^1 P_{30}+a_{50}^1 P_{50}\right)\left(1+F_{10}^{a1}\Delta\overline{F}\right)\left(1+r_{10}^{a1}P_{10}\right)\left(1+r_{10}^{c1}\cos\Omega_J\left(t_d-t_{10}^{c1}\right)\right)$$

$$\times\cos\omega'\left(t-t_{10}^{a1}\right)+\left(a_{32}^1 P_{31}+a_{52}^1 P_{52}\right)\cos\left[\omega'\left(t-t_{32}^{a1}\right)+2\lambda\right]$$

UT/longitude/magnetic activity

$$+\left(k_{21}^{a0}P_{21}+k_{41}^{a0}P_{41}+k_{61}^{a0}P_{61}\right)\left(1+r_{21}^{k0}P_{10}\right)\Delta A\cos\left(\lambda-\lambda_{21}^{k0}\right)$$

$$+k_{11}^{c1}P_{11}\cos\Omega_d\left(t_d-t_{10}^{c1}\right)\Delta A\cos\left(\lambda-\lambda_{11}^{kc}\right)$$

$$+\left[k_{10}^{a1}P_{10}+k_{30}^{a1}P_{30}+k_{50}^{a1}P_{50}\right]\Delta A\cos\omega'\left(t-t_{10}^{k1}\right) \tag{103}$$

$$F_1=1+F_{10}^c\Delta\overline{F}+f_{00}^{a1}\Delta F+f_{00}^{a2}\left(\Delta F\right)^2 \tag{104}$$

$$F_2 = 1 + F_{11}^a \Delta \overline{F} + f_{00}^{a1} \Delta F + f_{00}^{a2} (\Delta F)^2 \tag{105}$$

where

$$\Delta F = F_{10.7} - \overline{F}_{10.7} \qquad\qquad \Delta \overline{F} = \overline{F}_{10.7} - 150 \qquad\qquad \text{F10.7 is}$$

the solar flux measurement for the previous day, $\overline{F}_{10.7}$ is the 81day average of the solar flux

measurement centered on the day in question.

P_{nm} are the non normalized Legendre-associated functions equal to the following

$$\left[(1 - x^2)^{m/2} / 2^n n! \right] \left(d^{n+m} / dx^{n+m} \right) (x^2 - 1)^n$$

with x equal to the cosine of the geographic latitude,

$$\Omega_d = 2\pi/365 \qquad \omega = 2\pi/24 \qquad \omega' = 2\pi/86400, \ \tau \text{ is local time in hours, t is}$$

universal time in seconds, t_d is the day count in year, and λ is the geographic longitude

with eastward being positive. Hedin explains that there are two choices for magnetic

activity,

$$\Delta A = (Ap - 4) + (k_{00}^r - 1)\left\{ Ap - 4 + \left[\exp(-k_{00}^r (Ap - 4)) - 1 \right] / k_{00}^r \right\} \tag{106}$$

where Ap is the daily magnetic index, or there is another method illustrated that

establishes the magnetic activity that uses the average values over an extended period of

time. (Hedin, 1987, p. 4661)

III. ATMOSPHERIC MODEL EVALUATION

The evaluation of atmospheric drag models is a relatively difficult procedure owing to the fact that there is no real comparison tool to be used. Until enough satellites can be placed into various orbits and each of these satellites carries density measuring equipment, the density of a particular orbit cannot truly be obtained. As mentioned previously, the modeling of the earth's atmosphere is the most inaccurate of all the perturbations encountered in orbital motion analysis. The intent of this project was to obtain known vectors of a particular satellite program, and run a comparison of an orbital prediction scheme using each of three atmospheric models for two different altitudes. In order to make the comparison valid, consistency of the prediction scheme had to be verified.

The vectors being used in the analysis were obtained from the Air Force Satellite Tracking Center on two satellites, one at 650 kilometers and one at approximately 800 kilometers, both of which have a high inclination. The vectors, position and velocity represented in True of Date Cartesian coordinates, are obtained by triangulating the satellite position and predicting out to 20:00:00.00 local time. It would have been better for the evaluation, if the actual observed position of the satellites could have been obtained, but due to time constraints and logistical problems this could not be achieved. The accuracy of the position and velocity vectors is advertised by the STC to be within 2000 ft in the X, Y, and Z directions. It was decided at the time, that this accuracy was acceptable for the evaluation.

In order to provide consistency, the prediction scheme developed had to be the same as that used by the STC. This proved to be quite a troublesome problem. The STC uses a prediction scheme which models most if not all of the known perturbations. Depending on

47

what is requested, certain perturbations can be temporarily removed from the program. The vectors obtained from the STC contained only those perturbations which were inherent to the prediction scheme developed, with one exception. As mentioned previously, the STC uses the WGS-84 geopotential model. A great deal of effort was placed on placing the same geopotential model in the developed prediction scheme, but several problems soon became apparent. The conversion of True of Date coordinates into the WGS-84 frame of reference is not a trivial process. An attempt was made to incorporate the full 41 by 41 geopotential matrix in the scheme, but error build up and computational time increased greatly. It was decided to incorporate a truncated version of the WGS-84 geopotential model. A six by six matrix representing the first six zonals of the model was eventually used to prevent error build up. Future work on this project would have to include the conversion of the TOD coordinates to the WGS frame of reference and incorporation of the full 41 by 41 matrix.

Another way that consistency was achieved was to verify and use astrodynamical constants consistent with AIAA standards. Depending on which reference one uses to obtain values such as the earth's gravitational parameter, earth's equatorial radius, earth flattening constant and others, these values would all vary by some small amount. It was found that depending on which constant was used, the error would be different. It was decided to use the AIAA published values whenever possible. These values were placed in a subroutine of the prediction scheme to be used as necessary.

Once it had been determined that the developed prediction scheme was an equal representation of the STC's prediction scheme, or as close as it could be gotten in the time allowed, the model evaluation was begun. The vectors obtained from the STC spanned the time frame from 21 August 1993 to 22 September 1993 in 24 hour forecasts. That is, the position and velocity were reported for 20:00:00.00 of each day. These vectors were

48

then programmed into 60 satellite files, 30 for the 650 kilometer satellite and 30 for the 800 kilometer satellite. Each of the satellite files contains not only the position and velocity vectors, but also the environmental conditions of F10.7 and Ap for that day, plus the 81 day average F10.7 as reported by the National Geophysical Data Center. The vectors were propagated over a 24 hour period and compared to the next day's vector. Since the baseline vectors themselves contained error, it was decided to compare the results by using the specific mechanical energy, a conserved quantity, of each of the satellites over the 30 day period. By converting the position and velocity of the STC vectors and those obtained from the developed prediction scheme into specific mechanical energy using equation 107, a comparison could be made.

$$E = \frac{v^2}{2} - \frac{\mu}{r} \qquad (107)$$

A relative comparison of the position, velocity, right ascension, declination, and radial distance was then conducted in order to determine which model provided the most accurate results, the object being to meet or beat the 2000 foot accuracy advertised by the STC prediction scheme.

As mentioned, the evaluation procedure consisted of propagating the baseline vector for a 24 hour integration period for each of the satellites, then switching atmospheres and running the routine again. It must be noted that the Jacchia 60 and Jacchia 71 models were run with relatively little difficulty. The MSIS 86 atmospheric model proved to be quite the opposite. Due to an unexpected hardware failure late in the project, and the fact that the atmospheric model itself is quite difficult to integrate into the prediction scheme, the evaluation of this model could not be completed in time. Work is currently under way to correct this situation.

A. JACCHIA 60 MODEL EVALUATION

The first evaluation was conducted on the Jacchia 60 earth atmospheric model. The first procedure was to determine the values for the solar flux and geomagnetic activity encountered during the time period between August 21 to September 22, 1993. Figure 13 shows the reported values of F10.7 and Ap for this time period. As compared to Figure 6, it can be seen that the solar flux values are on the low side of the solar cycle, and the geomagnetic activity is relatively low. This allows for an easier comparison, because a perturbed atmosphere would have made some of the data points obtained during an active period out of range of those obtained during a quiet period.

The first evaluation was conducted on the satellite at 650 kilometers. Figure 14 illustrates the specific mechanical energy of the STC reported vectors versus the predicted vectors. It can be seen that the predicted vectors are extremely close to that of the STC reported values. The two error bars located on the graph illustrate the 2000 ft error range advertised by the STC prediction scheme. In one case it was found that the STC obtained vector on Julian date 242 was actually reported incorrectly. For the most part, however, the predicted values showed only small variations with the baseline vectors. In-track errors fell within the range of 1700 to 9000 feet in radial distance, and 0.01 to 0.15 degrees in declination. Cross-track errors also fell within the range of 0.01 to 0.15 degrees. Satellite velocities had some small error in the range of 0.2 to ten feet per second.

The same procedure was then conducted on the 800 kilometer satellite vectors. Once again the prediction scheme provided vectors very similar to those obtained from the STC. Figure 15 illustrates the results. It must be noted at this point, that the accuracy of the prediction scheme suffered at the higher altitude. This is due to the atmospheric model. As mentioned previously, accuracy of the atmospheric model deteriorates the

higher the altitude. In-track errors were found to range from 2500 to 9000 feet in radial distance, and 0.01 to 0.2 degrees in declination. Cross-track errors were in the range of 0.01 to 0.8 degrees. Velocity was in the range of one to eight feet per second.

B. JACCHIA 71 MODEL EVALUATION

Once again the procedure was run, this time with the Jacchia 71 model inserted into the prediction scheme. Figure 16 illustrates the results of the prediction runs on the 650 kilometer satellite. The prediction scheme provided very little variation with the baseline vectors. The in-track errors were 250 to 8000 feet in radial distance and 0.001 to 0.14 degrees in declination. Cross-track errors were also 0.001 to 0.14 degrees in right ascension. Errors in velocity predicted were 0.1 to ten feet per second. The results of this atmosphere at 650 kilometers were much more accurate than those of the Jacchia 60 model. In order to confirm this, the prediction scheme was run again with the vectors of the 850 kilometer satellite. In-track errors were in the range of 200 to 8000 feet in radial range and 0.001 to 0.10 degrees in declination. Cross-track errors were also comparable with the error range being 0.001 to 0.10 degrees of right ascension. This confirmed the fact that the Jacchia 71 model provided better accuracy at both altitudes. This is due to the fact that the Jacchia 71 model provides a more accurate modeling of the polar regions, whereas the Jacchia 60 does not model the polar regions as well. The modeling of the polar regions is extremely important for the satellite program being studied due to its high inclination.

IV. SUMMARY

This thesis has attempted to provide the underlying principles used in orbital prediction and a comparison of atmospheric models. The prediction scheme that has been created was used to compare the Jacchia 60 and Jacchia 71 earth atmospheric models. It was found that the Jacchia 71 model provided much more accurate results than the Jacchia 60. This would stand to reason due to the fact that the J71 model had a bigger data base with which to work from. The J71 model provides density information that is dependent both on solar activity as well as geomagnetic activity, whereas the J60 only relies on solar activity. The J71 also models the polar regions, which is essential to the satellite program being investigated. The MSIS 86 earth atmospheric model could not be compared due to time constraints, but is currently being integrated into the prediction scheme.

Several improvements can be made to the prediction scheme in order to improve accuracy. As discussed earlier, the geopotential model needs to be incorporated. The True of Date coordinates need to be transferred into the WGS-84 frame of reference, and the complete 41 by 41 geopotential matrix incorporated. Doing this would increase computational time, but accuracy would greatly improve. Another improvement in the prediction scheme would be to vary the B-factor as the satellite cross-sectional area changes through its orbital pass. Currently the B-factor is held at a constant value. By changing the B-factor as a function of latitude or declination, error can be reduced.

Follow on work on this project would include inserting other atmospheric models for comparison, such as the MSIS 86 and MSIS 90. Before doing this, however, it would be better if the satellite vectors being used were actual observations and not predictions themselves. This would provide a better realization of the accuracy of the program, and hence the atmospheric models. Another improvement in the program's accuracy would be to convert from True of Date Cartesian coordinates to normalized spherical coordinates and then integrate. Doing this would greatly decrease the error build up. As the

prediction scheme stands now, the error build-up causes accuracy problems if the vectors are integrated for more than a twenty four hour period.

Orbital prediction is an essential tool in today's space age. In the case of the satellite program of interest, if the accuracy of the orbital prediction can be improved, then the mission analysis can be improved. The interesting point of this project, was that the B-factor was no longer being used as the error catch-all. The B-factor for any given satellite can be correctly used, and the position and velocity as well as any other of the satellite ephemirides can be calculated. By incorporating more subroutines that model other perturbing forces, this prediction scheme can be used for other satellite programs.

APPENDIX A
FIGURES
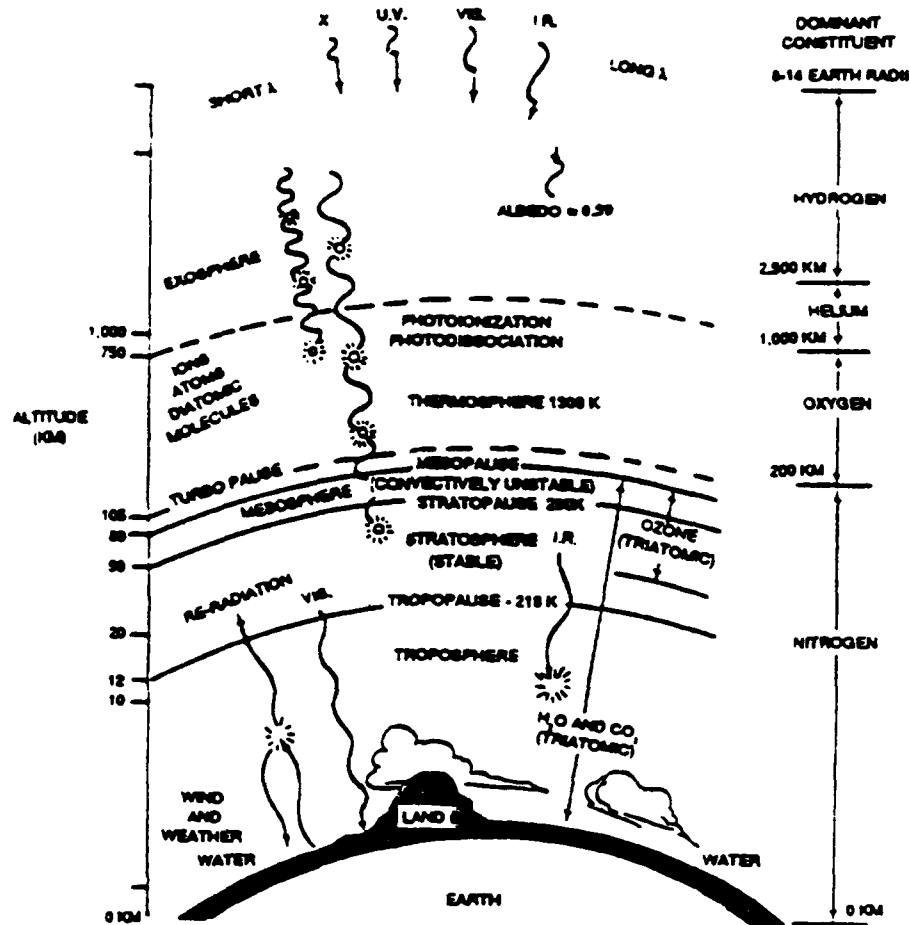
Figure 1. Atmosphere Breakdown
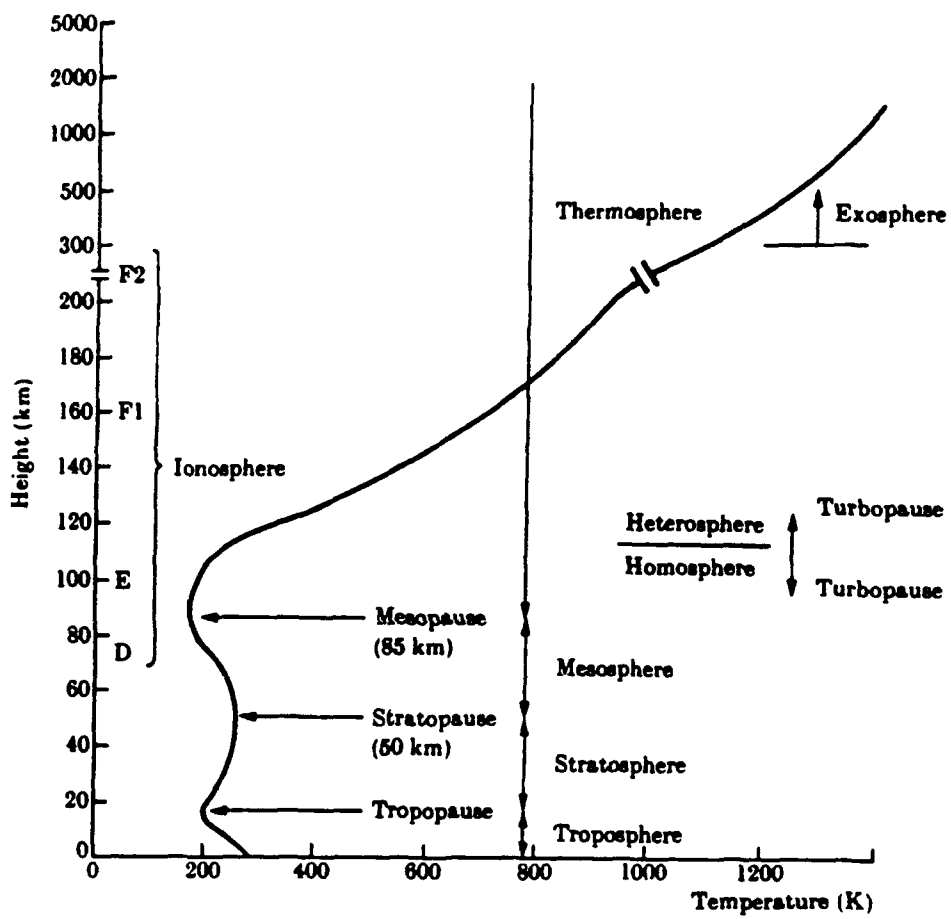
Figure 2. Temperature vs. Altitude
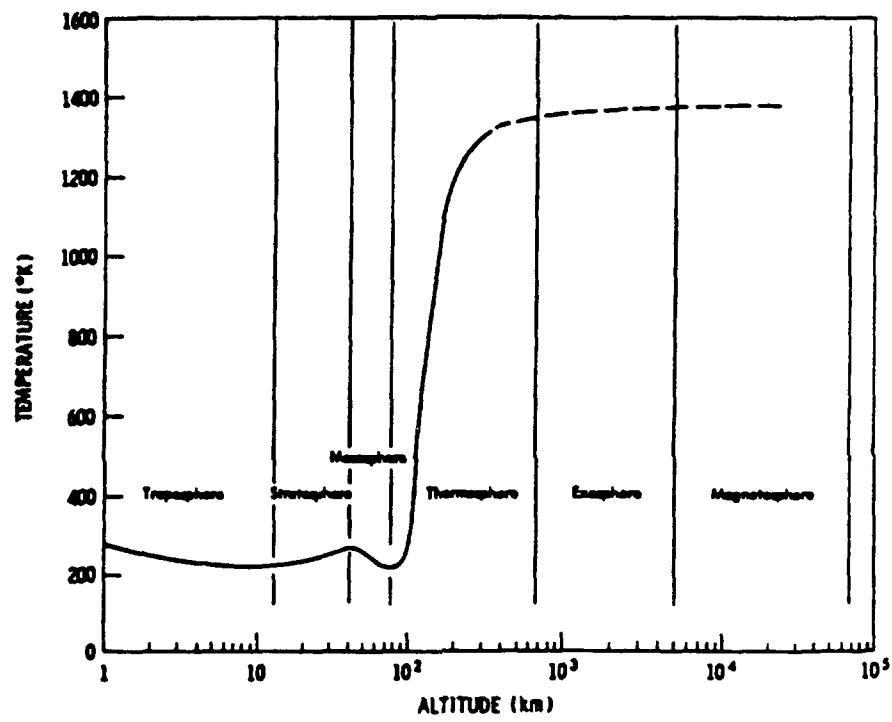
Figure 3. Temperature Profile of Earth's Atmosphere
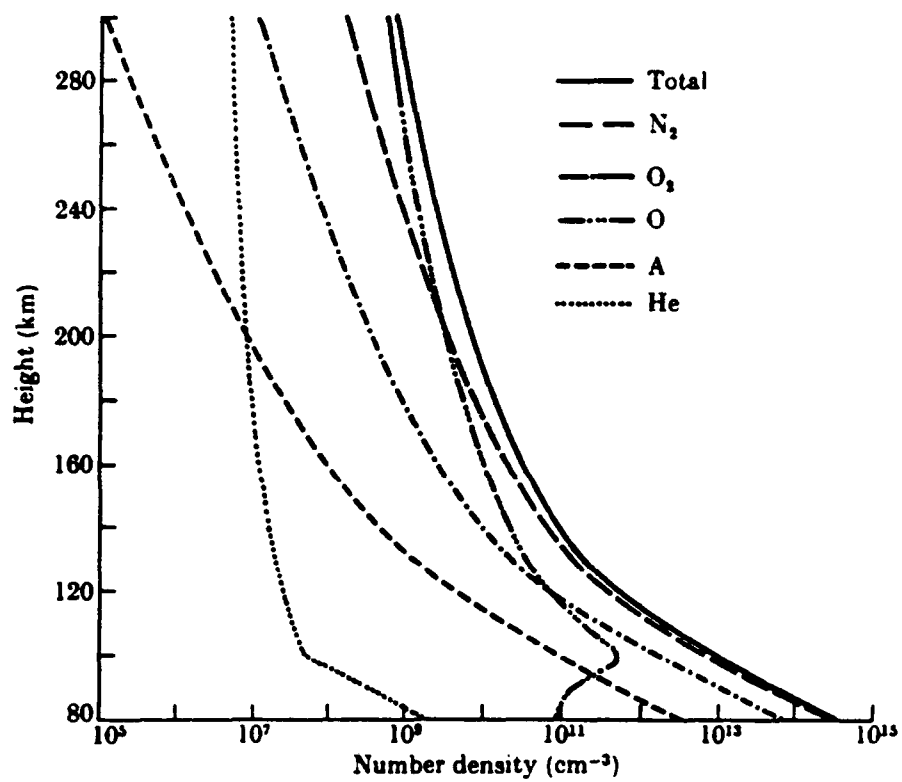
Figure 4. Height Variation of Number Density
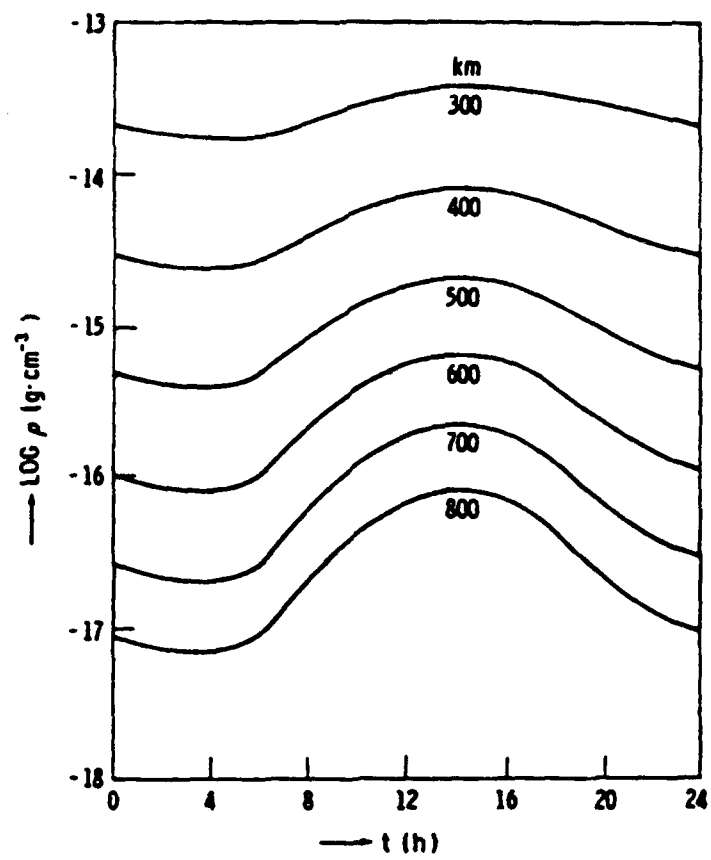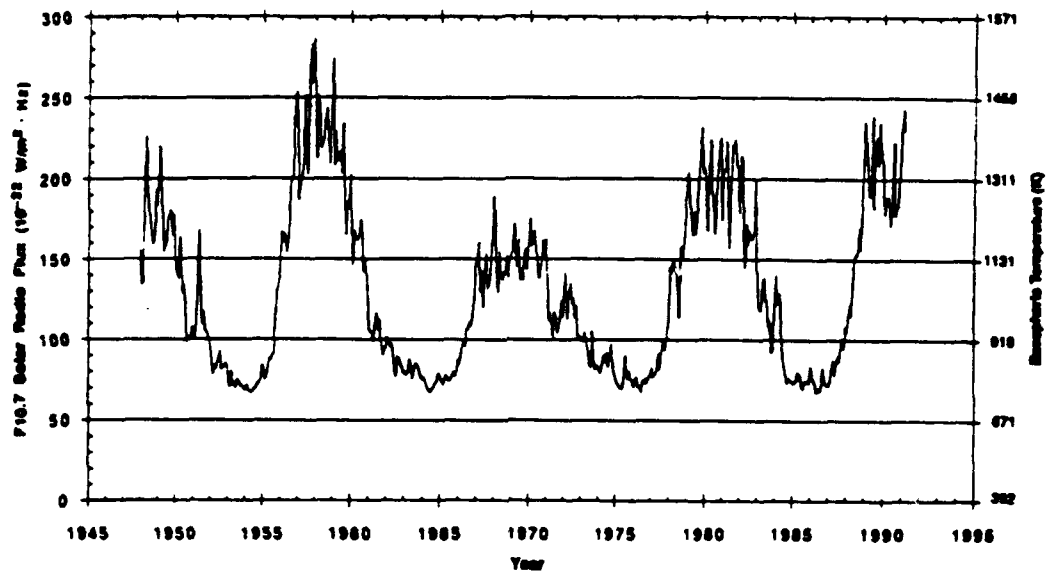
Figure 5. Diurnal Variation in Density
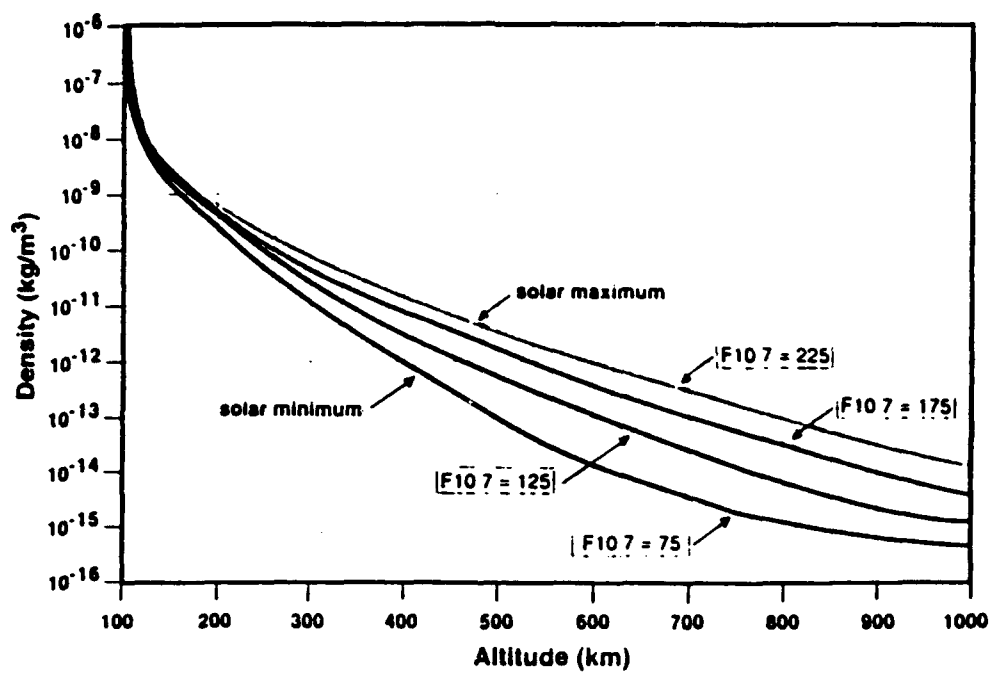
Figure 6. Solar Flux History

59

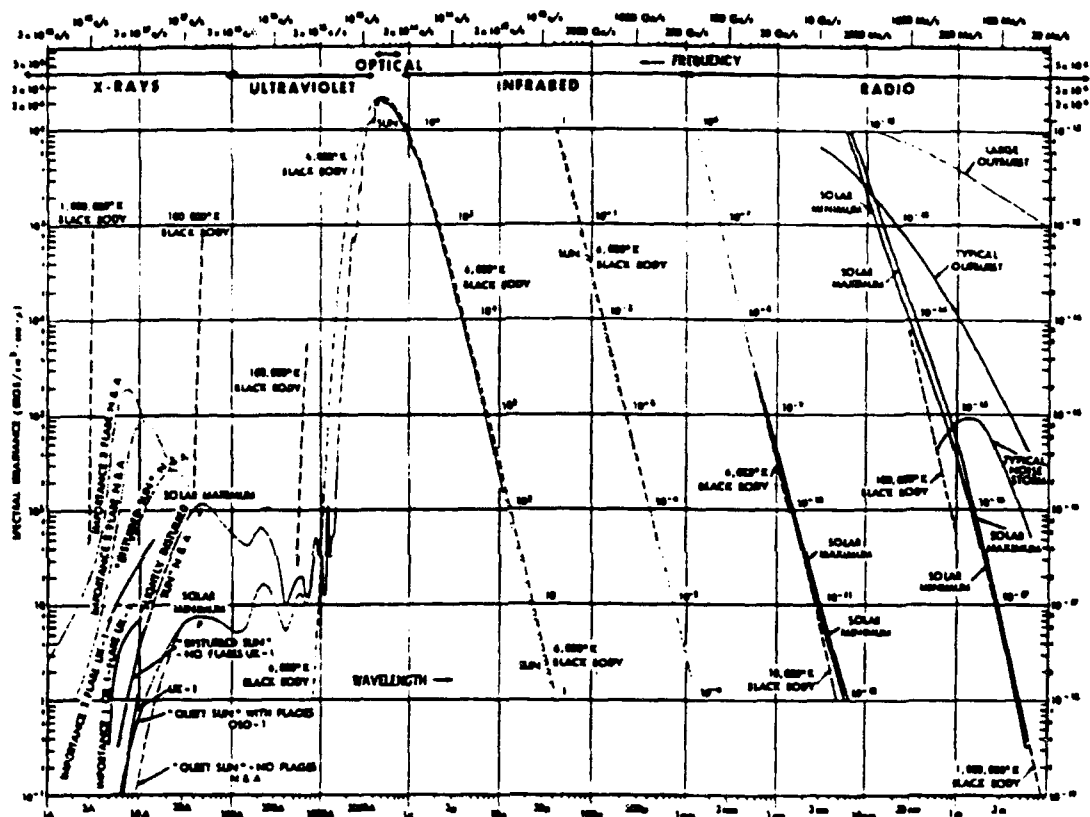Figure 7. Density vs. Altitude for Various F10.7 Values
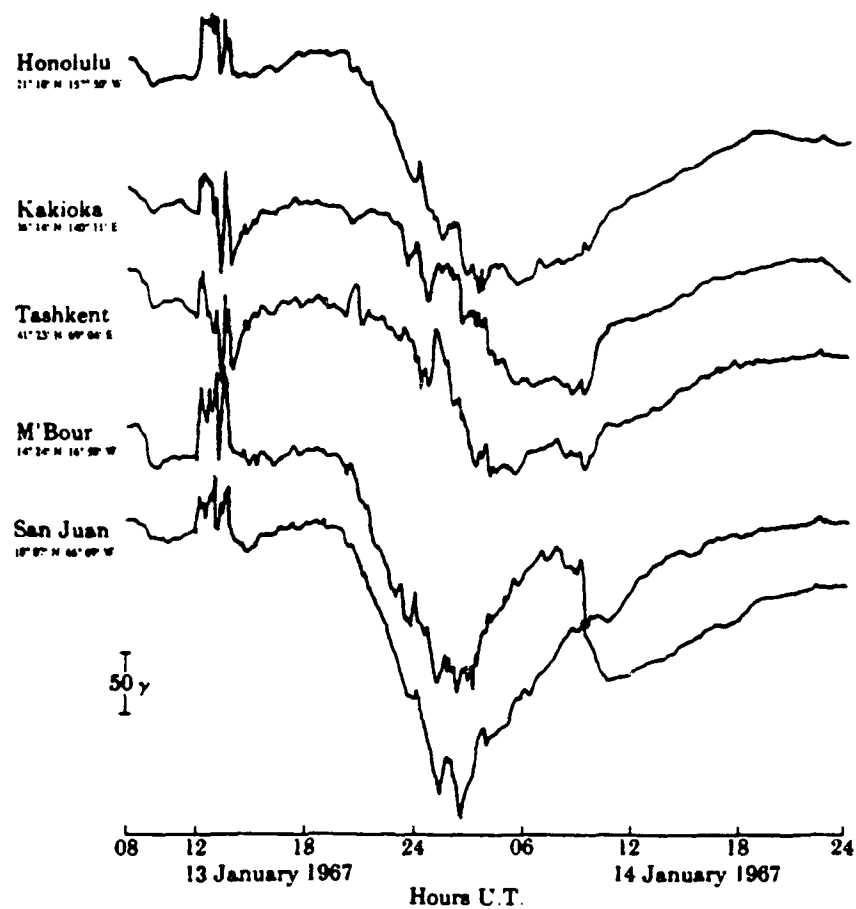
Figure 8. Solar Radiation Spectrum

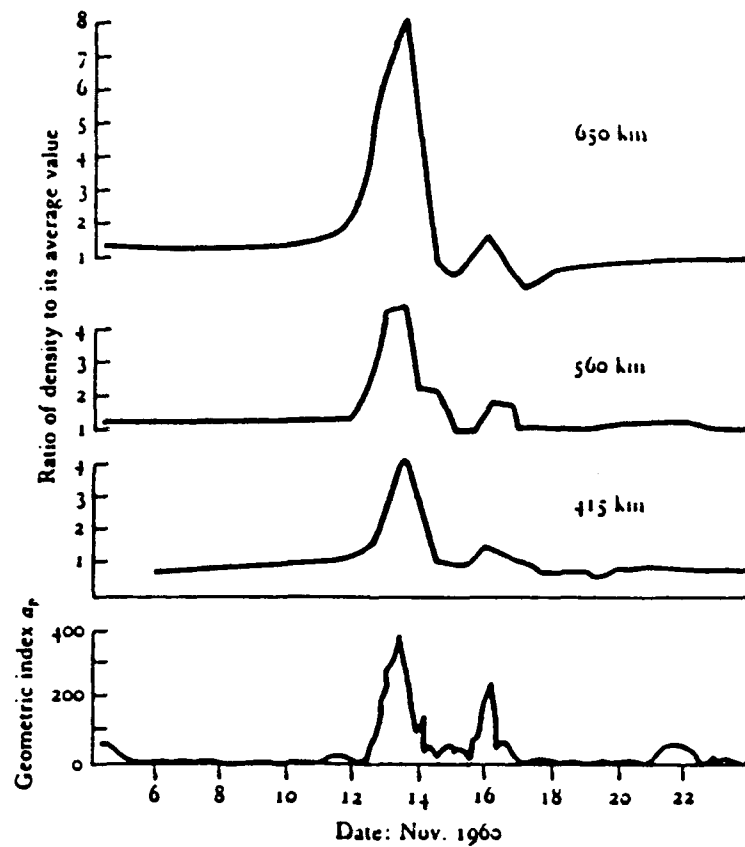Figure 9. Geomagnetic Storm Recording
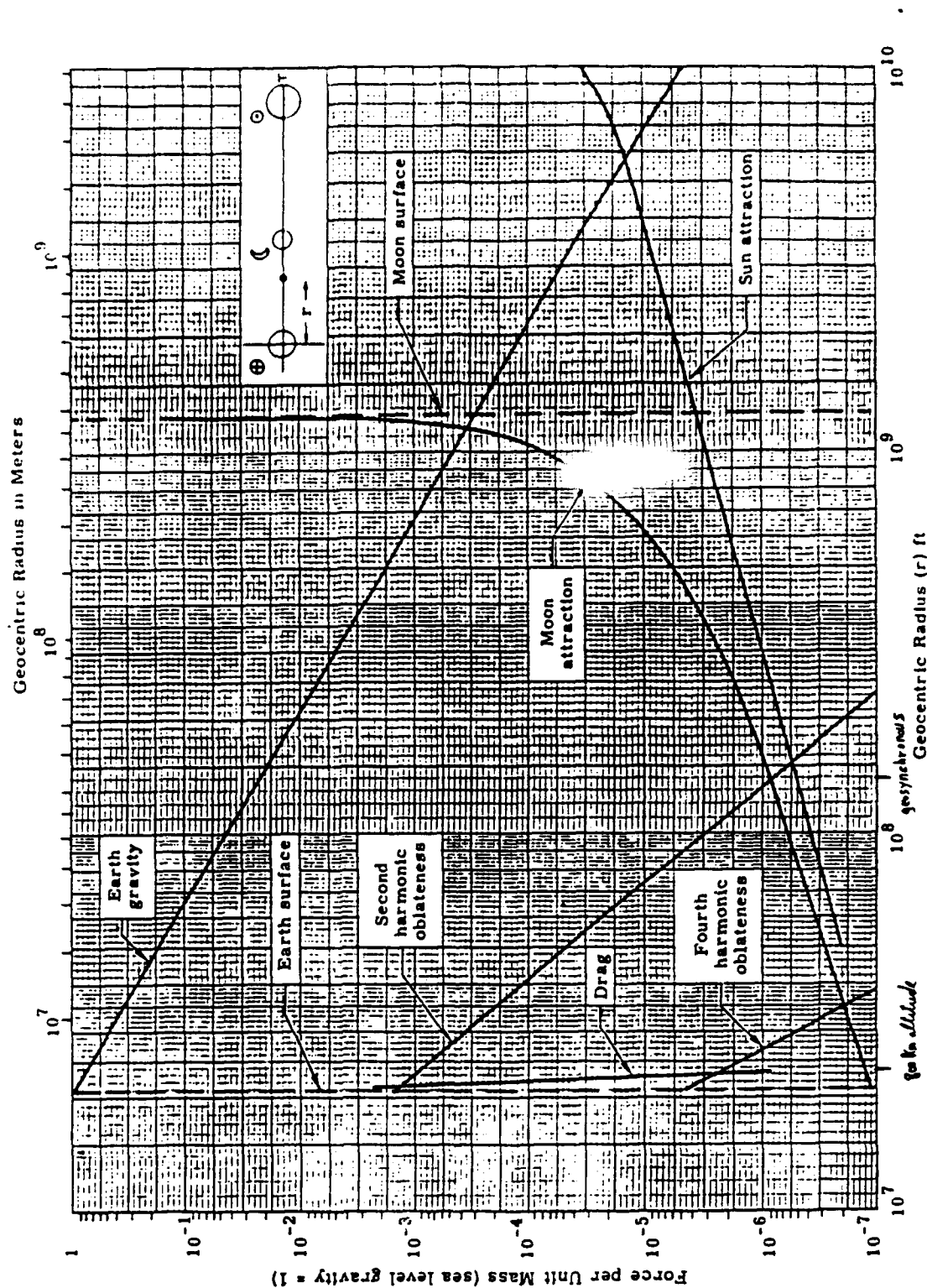
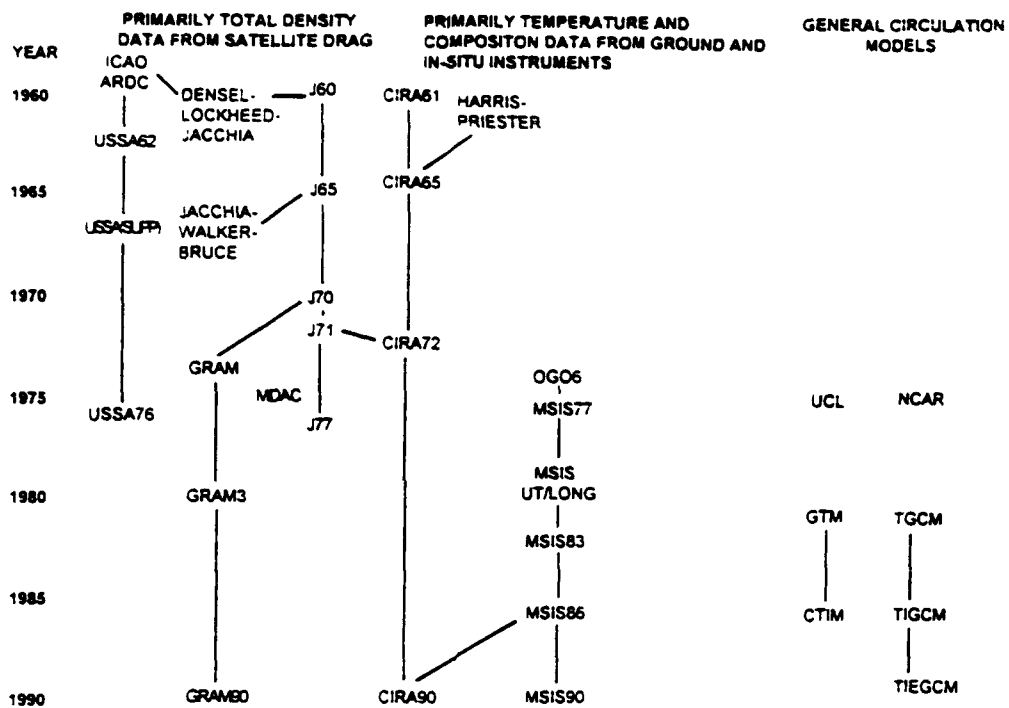Figure 10. Density vs. Altitude for Geomagnetic Storm

Figure 11. Comparison of Perturbation Magnitudes
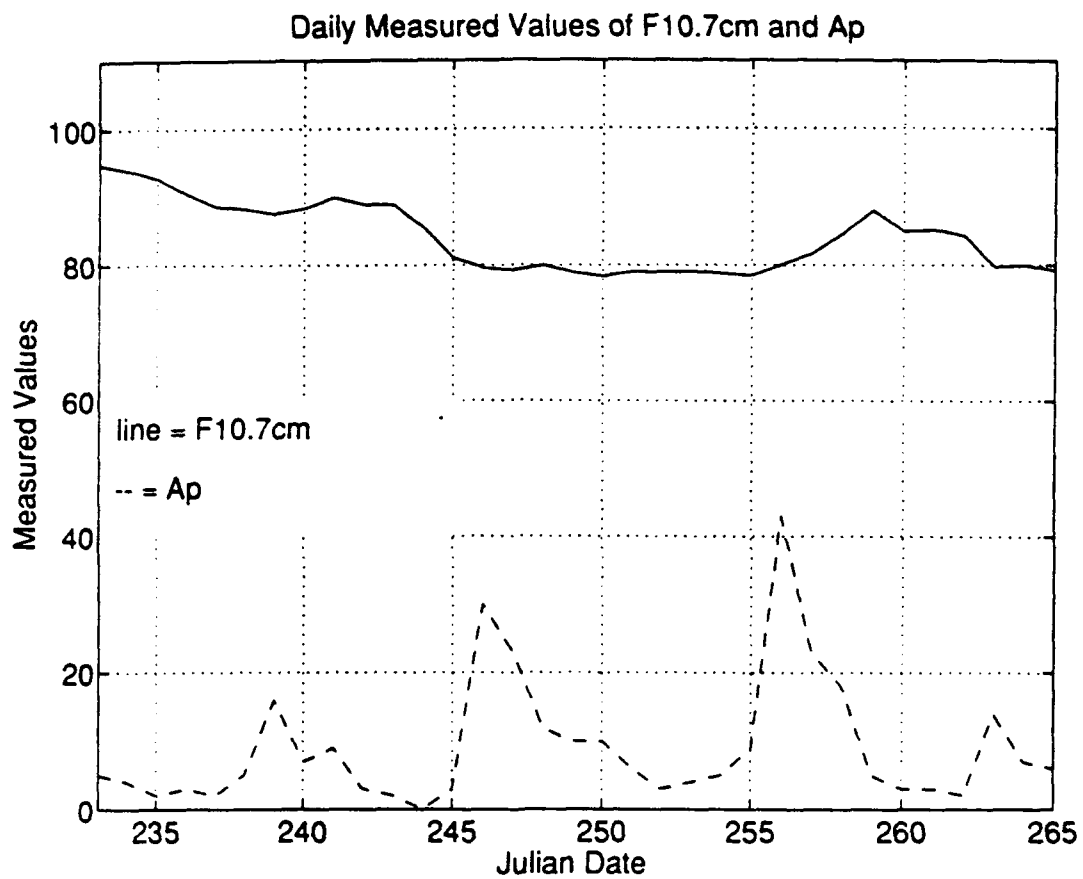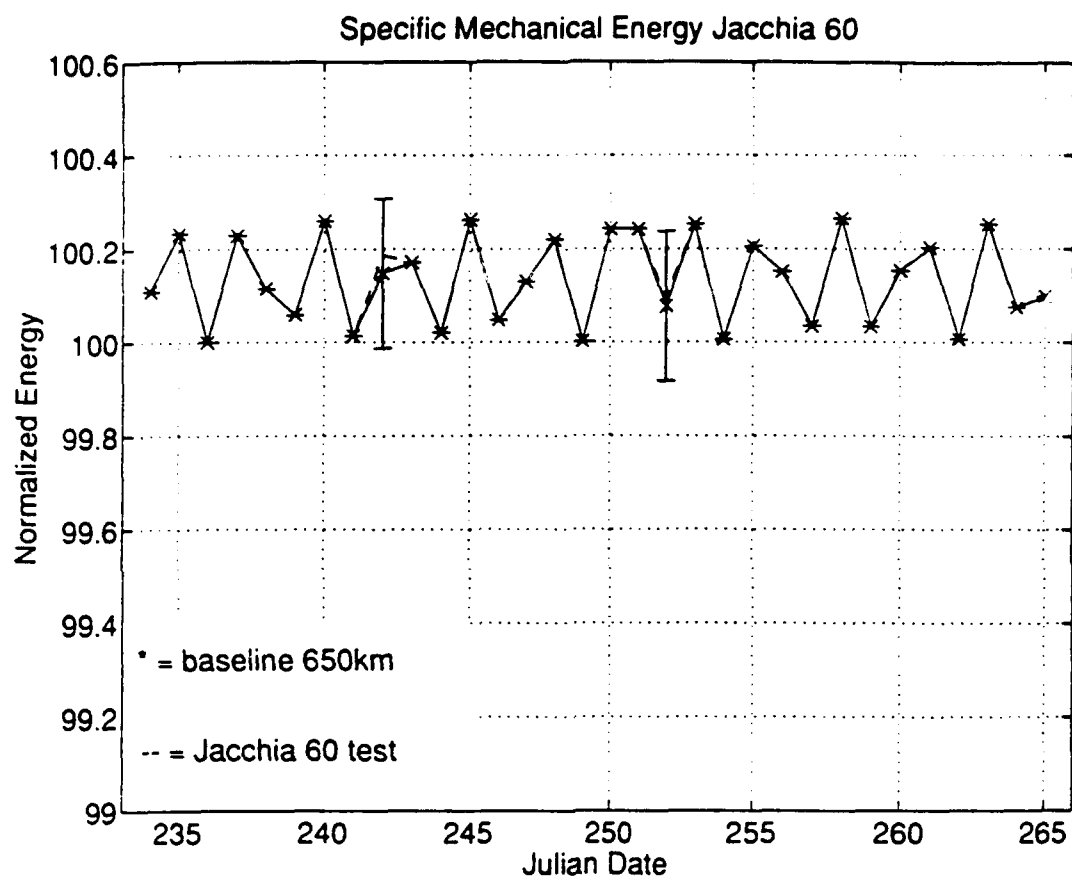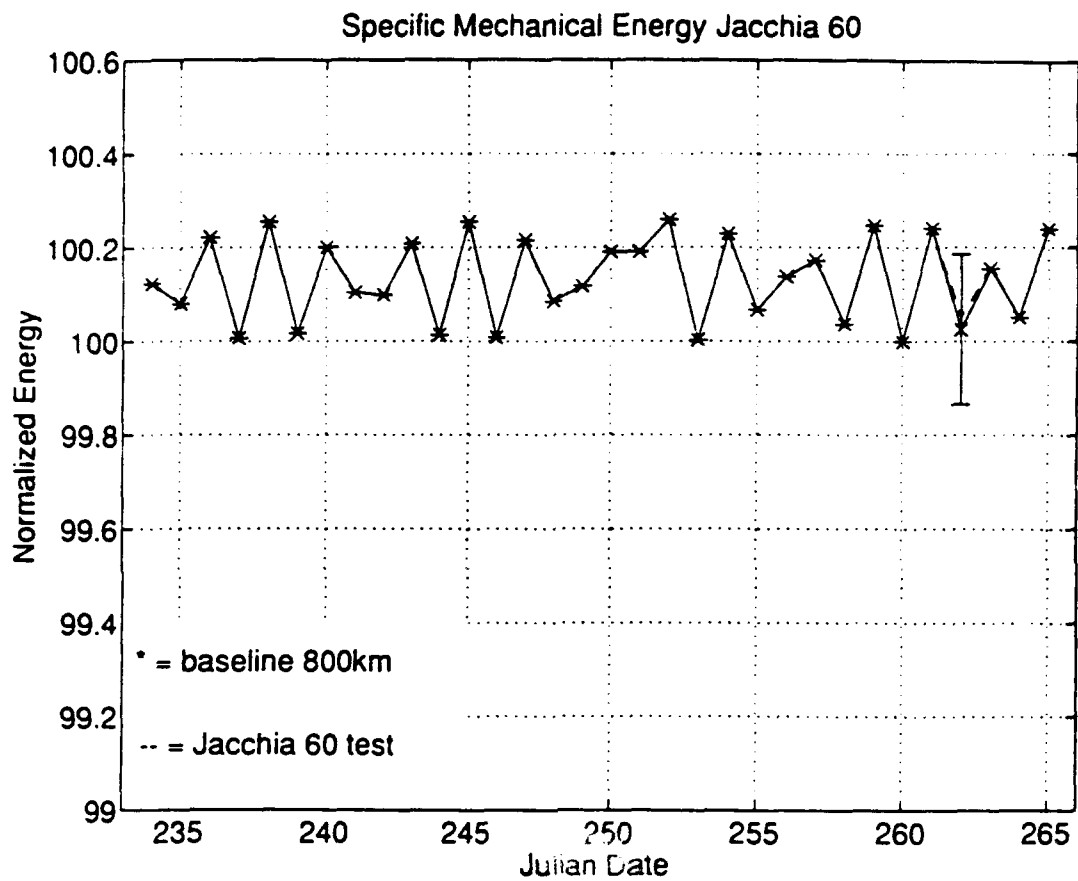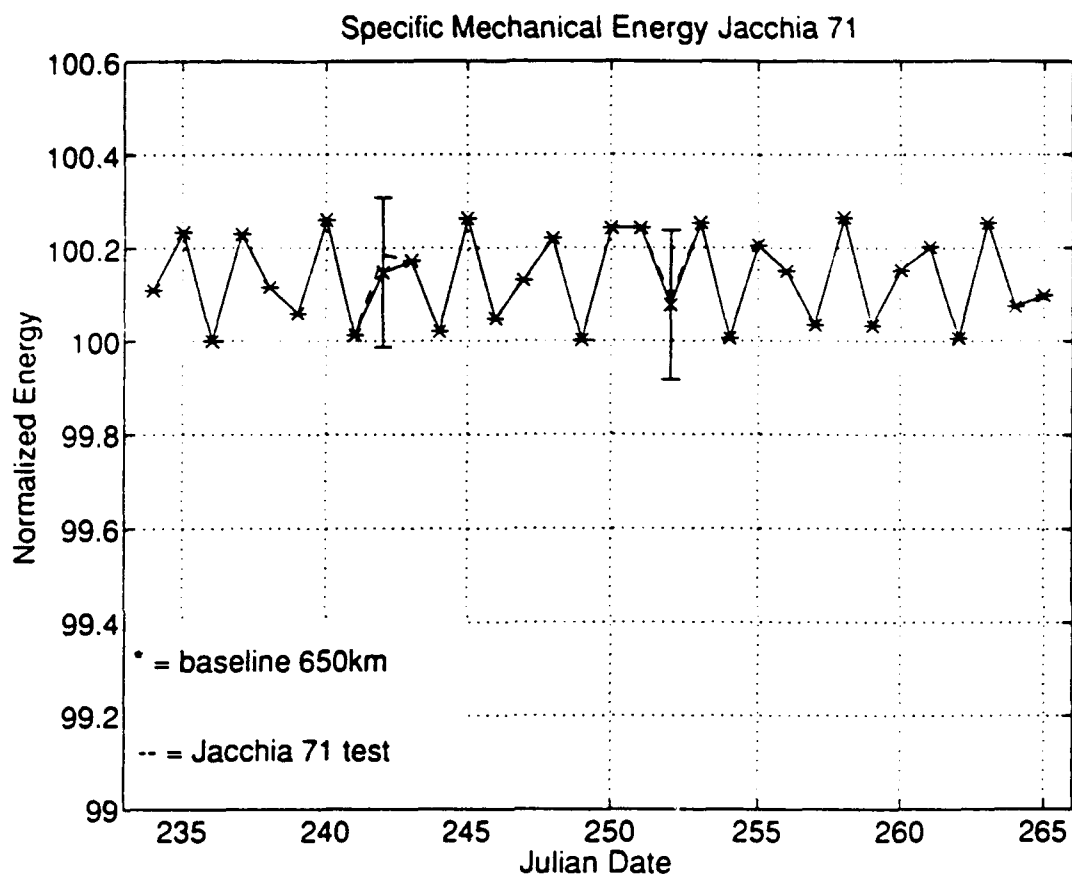
Figure 12. Atmospheric Model History

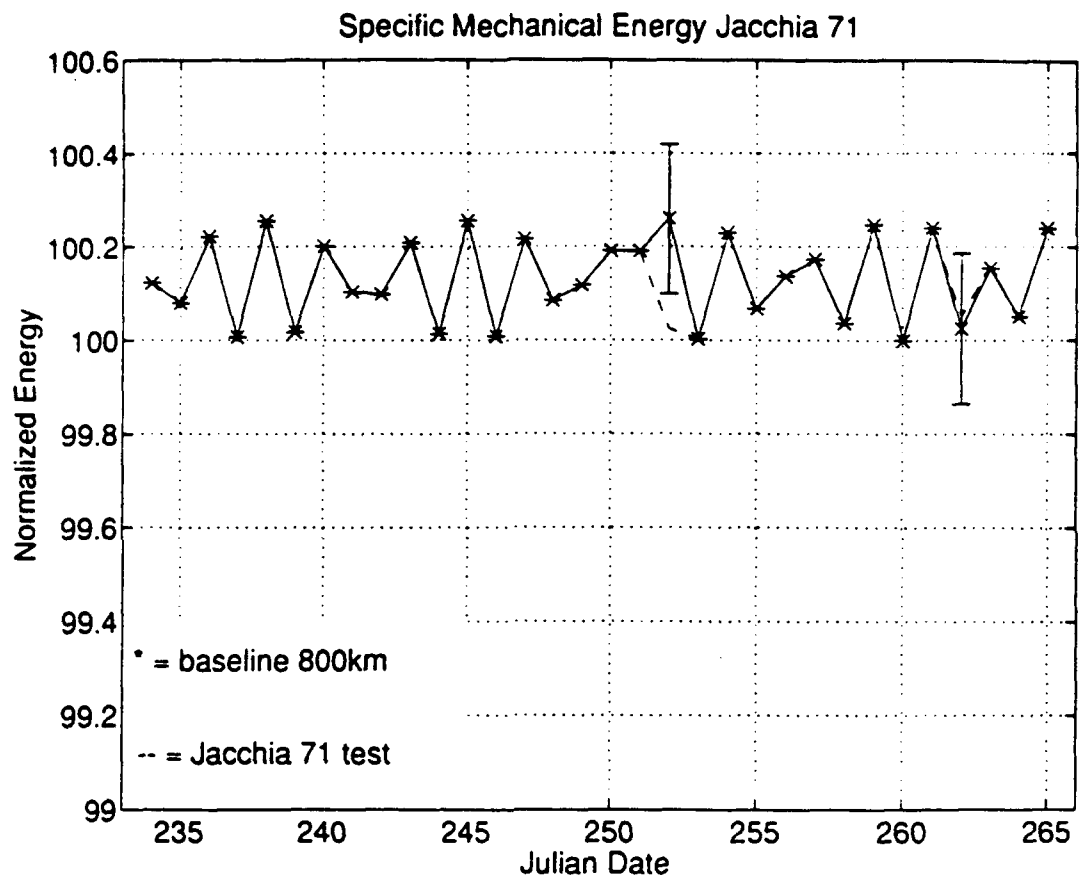Figure 13. Observed values of F10.7 and Ap for 21 August to 22 September 1993

Figure 14. Jacchia 60 Evaluation at 650 km

67

Figure 15. Jacchia 60 Evaluation at 800 km

Figure 16. Jacchia 71 Evaluation at 650 km

Figure 17. Jacchia 71 Evaluation at 800 km

APPENDIX B
TABLES

TABLE 1: PERTURBATION ACCELERATIONS

Cause	Formula	Parameters (in CGS units)	Geostationary satellite $a = 42\,160$ km $d/m = 0.1$ cm^2 g^{-1} 0.00^n	Lageos $12\,270$ 0.00^n	Starlette ~ 7300 0.01	Seasat ~ 7100 0.2
(1) Earth's monopole	$\dfrac{GM_{\oplus}}{r^2}$	$GM_{\oplus} = 3.986 \times 10^{20}$	2.2×10^2	2.8×10^2	7.5×10^2	7.9×10^2
(2) Earth's oblateness	$3\dfrac{GM_{\oplus}}{r^2}\left(\dfrac{R_{\oplus}}{r}\right)^2 J_{20}$	$J_{20} = 4.84 \times 10^{-4}$ $R_{\oplus} = 6.378 \times 10^8$	7.4×10^{-1}	1.0×10^0	8.3×10	9.3×10
(2) Low-order geopotential harmonics e.g. $l = 2$, $m = 2$	$3\dfrac{GM_{\oplus} R_{\oplus}^2}{r^4} J_{22}$	$J_{22} = 2.81 \times 10^{-6}$	4.3×10^{-4}	6.0×10^{-4}	4.8×10^{-1}	5.4×10^{-1}
$l = 6$, $m = 6$	$7\dfrac{GM_{\oplus} R_{\oplus}^6}{r^8} J_{66}$	$J_{66} = 2.42 \times 10^{-7}$	4.5×10^{-10}	8.8×10^{-4}	5.6×10^{-3}	7.0×10^{-3}
(2) High-order geopotential harmonics e.g. $l = 18$, $m = 18$	$19\dfrac{GM_{\oplus} R_{\oplus}^{18}}{r^{20}} J_{1818}$	$J_{1818} = 1.8 \times 10^{-8}$	1.3×10^{-20}	6.9×10^{-10}	2.2×10^{-3}	3.9×10^{-3}
(3) Perturbation due to the Moon	$2\dfrac{GM_{\zeta}}{r_{\zeta}^3} r$	$M_{\zeta} = M_{\oplus} \cdot 81.3$ $r_{\zeta} = 3.8 \times 10^{10}$	7.3×10^{-4}	2.1×10^{-4}	1.3×10^{-4}	1.3×10^{-4}
(3) Perturbation due to the Sun	$2\dfrac{GM_{\odot}}{r_{\odot}^3} r$	$M_{\odot} = 3.29 \times 10^5 M_{\oplus}$ $r_{\odot} = 1.5 \times 10^{13}$	3.3×10^{-4}	9.6×10^{-5}	5.7×10^{-5}	5.6×10^{-5}
(3) Perturbation due to other planets (e.g. Venus)	$2\dfrac{GM_{\varphi}}{r_{\varphi}^3} r$	$M_{\varphi} = 0.82 M_{\oplus}$ $r_{\varphi} = 4 \times 10^{12}$	4.3×10^{-8}	1.3×10^{-8}	7.5×10^{-9}	7.3×10^{-9}
(4) Indirect oblation	$3 J_{20}\dfrac{GM_{\zeta}}{r_{\zeta}^2}\left(\dfrac{R_{\oplus}}{r_{\zeta}}\right)^2 \dfrac{M_{\zeta}}{M_{\oplus}}$		1.4×10^{-9}	1.4×10^{-9}	1.4×10^{-9}	1.4×10^{-9}
(5) General relativistic correction	$\dfrac{GM_{\oplus}}{r^2}\dfrac{GM_{\oplus}}{c^2}\dfrac{1}{r}$	$\dfrac{GM_{\oplus}}{c^2} = 0.44$	2.3×10^{-9}	9.5×10^{-8}	4.5×10^{-7}	4.9×10^{-7}
(6) Atmospheric drag	$\tfrac{1}{2} C_D \dfrac{d}{m} \rho v^2$	$C_D = 2-4$ $\rho = 0-10^{-10}$	0(?)	3×10^{-10}	7×10^{-4}	2×10^{-1}
(7) Solar radiation pressure	$\dfrac{d}{m}\dfrac{\Phi_{\odot}}{c}$	$\Phi_{\odot} = 1.38 \times 10^6$	4.6×10^{-6}	3.2×10^{-7}	4.6×10^{-7}	9.2×10^{-6}
(8) Earth's albedo radiation pressure	$\dfrac{d}{m}\dfrac{\Phi_{\odot}}{c} A_{\oplus}\left(\dfrac{R_{\oplus}}{r}\right)^2$	$A_{\oplus} = 0.4$	4.2×10^{-8}	3.4×10^{-8}	1.4×10^{-7}	3.0×10^{-6}
(9) Thermal emission	$\dfrac{4}{9}\dfrac{d}{m}\dfrac{\Phi_{\odot}}{c}\alpha\dfrac{\Delta J}{J_0}$	$\alpha = 0.4-0.7$ $\Delta J = 1-20^\circ$	9.5×10^{-8}	1.9×10^{-10}	2.7×10^{-10}	1.9×10^{-7}

71

TABLE 2: TYPICAL BALLISTIC COEFFICIENTS FOR LEO SATELLITES

Satellite	mass (kg)	Shape	Max. cross-sectional area (m²)	Min. cross-sectio-nal area (m²)	Drag coeffi-cient for max. cross. area	Drag coeffi-cient for min. cross. area	Max. ballistic coeffi-cient (kg/m²)	Min. ballistic coeffi-cient (kg/m²)	Type of Mission
Oscar-1	5	box	0 075	0.0584	4	2	42.8	16.7	comm.
Intercosmos-16	550	cylin.	2.7	3.16	2.67	2.1	82 9	76 3	scientific
Viking	277	octag.	2.25	0.833	4	2.6	128	30.8	scientific
Explorer-11	37	octag.	0.18	0.07	2.83	2.6	203	72 6	astronomy
Explorer-17	188.2	sphere	0 621	0.621	2	2	152	152	scientific
Space Telescope	11000	cylind. w/ arrays	112	14.3	3.33	4	192	29.5	astronomy
OSO-7	634	9-sided	1.05	0.5	3.67	2.9	437	165	solar phys.
OSO-8	1063	cylind. w/ arrays	5.99	1.81	3.76	4	147	47.2	solar phys.
Pegasus-3	10500	cylind. w/ arrays	264	14.5	3.3	4	181	12 1	scientific
Landsat-1	891	cylind. w/ arrays	10.4	1.81	3 4	4	123	25.2	remote sensing
ERS-1	2160	box w/ arrays	45.1	4	4	4	135	12.0	remote sensing
LDEF-1	9695	12-face cylind.	39	14.3	2.67	4	169	93.1	exper. platform
HEAO-2	3150	hexag. prism	13 9	4.52	2 83	4	174	80 1	astronomy
Vanguard-2	9.39	sphere	0 2	0.2	2	2	23.5	23.5	scientific
SkyLab	76136	cylind. w/ arrays	462	46.4	3 5	4	410	47.1	scientific
Echo-1	75.3	sphere	731	731	2	2	0.515	0.515	comm.
Extrema							437	0 515	

LIST OF REFERENCES

Adler, J.J., *Thermospheric Modeling Accuracies Using F10.7 and Ap*, M.S. Thesis, Naval Postgraduate School, Monterey California, December 1993.

Akasofu,S., Chapman,S., *Solar Terrestrial Physics*, Oxford University Press, 1972.

Bate, R.R., Mueller, D.D., White, J.E., *Fundamentals of Astrodynamics*, Dover Publications, Inc., 1971.

Burns, A.G., Killeen, T.L., *Changes of Neutral Composition in the Thermosphere*, AAS Publications Office, 1991.

Fleagle, R.G., Businger, J.A., *An Introduction to Atmospheric Physics*, Academic Press, 1963.

Hedin, A.E., et.al., *A Global Thermospheric Model Based on Mass Spectrometer and Incoherent Scatter Data; MSIS 1. N2 Density and Temperature*, Journal of Geophysical Research, Vol. 82, No. 16, 1977.

Hedin, A.E., et. al., *Global Model of Longitude/UT Variations in Thermospheric Composition and Temperature Based on Mass Spectrometer Data*, Journal of Geophysical Research, Vol. 84, No. A1, 1979.

Hedin, A.E., *MSIS-86 Thermospheric Model*, Journal of Geophysical Research, Vol. 92, No. A5, 1987.

Hess, W.N., *Introduction to Space Science*, Gordon and Breach, Science Publishers, 1968.

Jacchia, L.G., *New Static Models of the Thermosphere and Exosphere with Emperical Temperature Profiles*, Smithsonian Astrophysical Observatory, 1970.

Jacchia, L.G., *Variations in the Earth's Upper Atmosphere as Revealed by Satellite Drag*, Smithsonian Astrophysical Observatory, 1963.

Larson, W.J., Wertz, J.R., *Space Mission Analysis and Design*, 2nd Ed., Microcosm, Inc., 1992.

Lockheed, *Lockheed Working Papers*, 1992.

Marcos, F.A., et. al., *Satellite Drag Models: Current Status and Prospects*, AIAA, AAS Publications, 1993.

Milani, A., Nobili, A.M., Farinella, P., *Non-Gravitational Perurbations and Satellite Geodesy*, Adam Hilger, 1987.

Ratcliffe, J.A., *An Introduction to the Ionosphere and Magnetosphere*, Cambridge University Press, 1972.

Ross, I. M. AA4850:   1994.

U.S. Air Force, *Handbook of Geophysics*, The Macmillan Company, 1960.

INITIAL DISTRIBUTION LIST

No. Copies

1. Defense Technical Information Center 2
   Cameron Station
   Alexadria, Virginia 22304-6145

2. Library, Code 52 2
   Naval Postgraduate School
   Monterey, California 93943-5100

3. Department Chairman, Code AA 1
   Department of Aeronautics
   Naval Postgraduate School
   Monterey, California 93943-5000

4. SMC/IMO 1
   2420 Vela Way, Suite 1467
   Los Angeles AFB, Ca. 90245-4659
   Attn: Brig. Gen. Don Walker

5. Dr. R. C. Olsen 5
   Code PH/Ol
   Naval Postgraduate School
   Monterey, CA 93943-5002

6. Dr. I. M. Ross 1
   Code AA/Ro
   Naval Postgraduate School
   Monterey, CA 93943-5002

7. Dr. D. A. Danielson 1
   Code MA/Dd
   Naval Postgraduate School
   Monterey, CA 93943-5002

8. CDR. R. L. Wight 1
   Code Sp/Wt
   Naval Postgraduate School
   Monterey, CA 93943-5002

9.   LT Brian E. Bowden   5
       4089 Porte De Palmas #120
       San Diego, CA 92122